Recovery of absorbance spectra of micrometer-sized biological and inanimate particles

R. Lukacs[*1], R. Blümel[2] B. Zimmerman[1], M. Bağcıoğlu[1], and A. Kohler[1]

[1]Department of Mathematical Sciences and Technology, Faculty of Environmental Science and Technology, Norwegian University of Life Sciences, 1432 Ås, Norway

[2]Department of Physics, Wesleyan University, Middletown, Connecticut 06459-0155, USA

*Corresponding author:

Rozalia Lukacs,

Department of Mathematical Sciences and Technology (IMT),

Faculty of Environmental Science and Technology

Norwegian University of Life Sciences,

Drøbakveien 31, 1432 Ås, Norway

Tel: +47 64 96 54 29

Fax: +47 64 96 54 01

E-mail: rozalia.lukacs@nmbu.no

Abstract

In this paper, we first provide an overview of the Mie type scattering at absorbing materials and existing correction methods, followed by a new method to obtain the pure absorbance spectra of biological systems with spherical symmetry. This method is a further development of the recently described iterative algorithm of van Dijk et al. [1]. The method is tested on FTIR synchrotron spectra of *polymethyl methacrylate* (PMMA) microspheres and pollen grains with approximately spherical shape. The imaginary part of the refractive index was successfully recovered for both systems. Good agreement was obtained between the pure absorbance spectra obtained by this method and the measured spectra.

Key Words: **Mie scattering, ripples, FTIR spectroscopy**, **recovery of pure absorbance, PMMA**

1. Introduction

For several decades, infrared (IR) spectroscopy has been extensively applied within biological sciences to investigate more or less intact biochemical structures [2-4]. The main advantage of IR spectroscopy is that biological materials can be investigated without any extraction steps or chemical sample pre-treatment. Biochemical information on biological samples is obtained via interpretation of highly specific chemical absorption bands. Following the invention of Fourier transform IR (FTIR) microscopes in the 1980s [5], infrared spectroscopy experienced a further boost. As a consequence of this development, FTIR microspectroscopy of thin tissue sections gained in popularity. Compared to traditional microscopy, the advantage of FTIR microspectroscopy is that chemical information from intact tissue can be obtained without using staining of the tissue sections [6, 7]. Thin tissue sections for FTIR microspectroscopy have typical thickness of 6-10 μm, and can be obtained by cryo-sectioning. The thin sections are placed on infrared-transparent material and measured in transmission by infrared microspectroscopy. In addition, FTIR microspectroscopy has been used successfully for the investigation of single cells such as plant and human cells [8, 9].

Recently, synchrotron light sources have attracted considerable attention. While conventional light sources (black body radiators) have a higher total power in the infrared, synchrotron light sources are more strongly collimated, resulting in a higher brilliance in the infrared. This allows the use of aperture sizes down to a few microns.

Since tissue sections, cells and other biological materials vary strongly in size and morphology, FTIR spectroscopy and microspectroscopy are strongly hampered by non-chemical variations, such as scattering contributions, which often seriously distort pure chemical absorption spectra. The strongest non-chemical variations in the FTIR spectroscopy of thin dried films or tissue sections are due to differences in the sample thicknesses. When

the sample thickness changes the effective optical path length, a so-called multiplicative effect is present, which can effectively be estimated and suppressed by extended multiplicative signal correction (EMSC) [10]. Baseline variations, another non-chemical variation that are typical for FTIR microspectroscopy, arise when the light intensity varies, e.g. during the time interval between background and sample measurements. The resulting baseline variations are constant baseline shifts over the whole spectral region, and can equally well be estimated and suppressed by EMSC [10]. A third type of non-chemical variations, that are typical for the FTIR microspectroscopy of cells, are Mie-type scattering variations [11]. Scattering effects have been identified as a major obstacle for the reliable interpretation and further use of IR spectra in biological and biomedical science, and therefore methods for the recovery of pure absorbance spectra are needed.

Analytical solutions for the scattering of light at spheres are known and have for the first time been provided by Gustav Mie [12]. Mie-type scattering at cells causes strong and broad background oscillations, which can be effectively suppressed by EMSC, applying a meta-model of the analytical Mie solutions [13]. Subsequently, it has been pointed out that the broad oscillations caused by Mie scattering cannot be treated independently from chemical absorption in the FTIR microspectroscopy of single cells [14]. The real and the imaginary parts of the refractive index are determined by both optical and chemical properties of the material. Since the real and the imaginary parts of the refractive index are further related by the Kramers-Kronig relation [15, 16], they depend on each other and cannot be treated independently. Excellent reviews of the field of scattering in IR spectroscopy are available such as the recent review by Bhargava [17]. In this review the problem of the interdependence of sample geometry, optical properties of the FTIR spectrometer, and scattering and absorption is clearly outlined and the corresponding literature dealing with this complex issue is reviewed. The two additional papers of the Bhargava group, that include the optical

properties of the spectrometer, provide a general framework for scattering from layered samples [18] and spheres [19]. Therefore, while the general electromagnetic theory of the apparatus-sample interaction and its influence on the complex refractive index of the sample is known, the focus in this paper is on a concrete problem. Namely the question of whether scattering (real part of the refractive index) and absorption (imaginary part of the refractive index) may be treated independently in some geometries. The results of our study show that state-of-the-art models describing Mie-type scattering and absorption deviate considerably from the exact results.

Several approximate models have been established to explain Mie-type scattering and absorption of FTIR spectroscopy of cells and tissues [14, 20-24]. As we will see, the problem is complicated, and existing modelling algorithms and software are not yet completely up to the task. Kohler et al. [13] and Bassan et al. [20-22] suggested an algorithm based on multiplicative signal correction [25]. They used the van de Hulst approximation formula for the calculation of the Mie scattering efficiency [26]. This equation is an approximation used instead of the full Mie theory. While the approach is very efficient, it represents only a rough estimate since it uses an approximation formula for the non-absorbing case and no numerical aperture is considered.

Recently Van Dijck et al. [1] suggested a method for the recovery of the complex refractive index of materials with spherical shape. The effects of the sample morphology on the measured spectra can be removed, and using the imaginary part of the index, the shape-independent IR absorption spectrum of the material is recovered. The authors have applied their algorithm to polymethyl methacrylate (PMMA) spheres. The size of the PMMA spheres is a required input parameter for their algorithm. In case the size of the spherical object is not known *a priori*, the authors have suggested using the spectral region 2000-2600 cm^{-1} to obtain an estimate of the size of the sphere. In the present paper we evaluate this strategy for

biological samples. We combine the method suggested by Van Dijck et al. with EMSC, and develop an algorithm that allows recovering the pure absorbance spectra of biological systems in the presence of Mie type scattering. Since the development of future inverse scattering algorithms will benefit from any simplifying property of the scattering system, we first investigate and answer the question to what extent scattering and absorption can be treated independently. We then investigate the recovery of spectra for two separate systems, PMMA spheres and pollen. Pollen grains are a very close approximation of biological Mie scatter systems since they may have spheroidal shapes. By investigating this relatively simple system we may, in the future, generalize the method for more complicated biological systems such as cells.

Our paper is organized in the following way. In the section “Theory” we set the stage by introducing our notation and theoretical background used and applied in our paper. In section “Experiment” we provide the experimental details of the synchrotron FTIR measurements. In section “Results and Discussion” we show that in the case of absorbing spheres the assumption of independence of scattering and absorption is not justified. We find that current state-of-the art models [see e.g. Kohler et al. [13] and Bassan et al. [20]] may predict spurious line shifts of up to 12 cm^{-1}. Therefore the models that employ independence of scattering and absorption need to be improved. We present our algorithm for the recovery of pure absorbance spectra of two systems: 1) a model system (PMMA spheres), and 2) a biological system (pollen grains with approximately spherical shapes). In some of our model calculations we need to model chemical absorption lines, and this we do by using the Lorentz model discussed in detail in Appendix A. There is an additional reason for presenting the Lorentz model in Appendix A: There is tremendous, as yet untapped, potential in the Lorentz model for extracting pure absorbance spectra. This is so, since (i) absorption bands, in principle, can be traced back to their molecular origins and (ii) the absorption lines described

in the Lorentz model automatically satisfy the Kramers Kronig relation [15, 16]. This may be put to use in the construction of forward models for scattering on isolated scatterers such as cells or other micron-sized biological samples. In Appendix B we provide the analytical solutions for Mie scattering that introduces the notation. It shows that the analytical scattering and extinction formulas for dielectric spheres can be stated in compact form. In addition, the formulas may be used as a basis for the extraction of pure absorbance spectra from (approximately) spherical scatterers of a biological or inanimate nature.

2. Theory

The purpose of this section is to present the theoretical concepts and algorithms used, applied, and referred to in our paper. In subsection 'Basic definitions' we start with some basic definitions to set the stage and to introduce our notation. In subsection 'Mie scattering' we discuss scattering at an absorbing sphere and we show a possible way to calculate the absorbance when the numerical aperture of the optical system is included. In subsection 'Iterative algorithm' we present the steps of the algorithm proposed by van Dijck et al.

Basic definitions

In the infrared spectroscopy of biological materials, measurements are usually performed in forward direction. As illustrated in Fig. 1, infrared light impinges on a cell or a film of biological material representing a scatterer. The incident intensity is denoted by I_0; it is usually referred to as the reference intensity and it is characteristic for the light source. It is experimentally obtained by moving the scatterer out of the light path. Part of the incident light I_0 may be scattered, as illustrated by the blue arrows in Fig. 1; it may be absorbed by the scatterer, as illustrated by the red area, which denotes a radiation sink; and it may be transmitted, as illustrated by the purple arrows. The transmitted beam is recorded by the

detector as the sample intensity *I*. The intensity *I* is directly proportional to the power $\wp$ measured by the detector. It is given by $\wp = IG$, where *G* is the area of the aperture in front of the detector (see Fig. 1). Along the same lines both the scattered power and the absorbed power can be expressed in the following way: The scattered power $\wp_{sca}$ is given by $\wp_{sca} = I_0\,\sigma_{sca}$ and the absorbed power is given by $\wp_{abs} = I_0\,\sigma_{abs}$, hereby defining the cross sections σ_{sca} and σ_{abs} for scattering and absorption, respectively. Denoting by $\wp_0 = I_0 G$ the power recorded by the detector in the absence of the scatterer, the balance of power requires

$$\wp_0 = \wp + \wp_{sca} + \wp_{abs} \qquad (1)$$

With this equation, the transmission, defined as

$$T = \frac{I}{I_0} \quad (2)$$

may also be written as

$$T = 1 - \frac{\sigma_{ext}}{G}, \quad (3)$$

where $\sigma_{ext} = \sigma_{sca} + \sigma_{abs}$ is the extinction cross section. A commonly used quantity is the dimensionless extinction efficiency Q_{ext} , which is defined as

$$Q_{ext} = \frac{\sigma_{ext}}{g} \qquad (4)$$

where g is the geometrical cross section of the scatterer. Conventionally, in chemistry, a quantity called absorbance *A* is defined as

$$A = -\log_{10}(T). \qquad (5)$$

The following formulas are useful, since they allow us to go back and forth between *A* and Q_{ext}. For given *A* we obtain Q_{ext} according to

$$Q_{ext} = [1 - 10^{-A}]\frac{G}{g} \quad (6)$$

and for given Q_{ext} we obtain A according to

$$A = -\log_{10}\left[1 - \frac{g}{G}Q_{ext}\right] \qquad (7)$$

Only in the case where σ_{sca} is very small compared to σ_{abs}, are A and T simply related to σ_{abs}. In this case, with Eq. 3, we obtain

$$T \approx 1 - \frac{\sigma_{abs}}{G}. \quad (8)$$

As before, A is obtained according to Eq. 5. All these quantities are frequency dependent and usually given as a function of the wavenumber $\tilde{\nu}$, which is the reciprocal of the wavelength λ.

Equation 3 is a ray-optical result and valid only if diffraction at the detector aperture is negligible. This requires that both dimensions of G are much larger than λ. In addition, G has to be large compared with σ_{ext}. This is readily apparent from Eq. 3, which predicts the nonsensical result $T<0$ for $G < \sigma_{ext}$. Here, we are using the correct value of σ_{ext}, determined in an experiment with sufficiently large G. If, however, we measure σ_{ext} with a G that approaches σ_{ext} in size, and since T cannot be negative, the measured σ_{ext}, in this case, will differ from its asymptotic value obtained using a large G. This discussion acquires immediate relevance in the context of synchrotron light scattering, where the width of the incident beam may be of the order of, or narrower than, the size of the scattering particle, thus substantially modifying σ_{ext}. This may occur, e.g., when strongly focused synchrotron light is used in the study of single biological cells.

A further important comment concerns the refractive index, which is an important quantity when considering the scattering of light at biological materials. Since biological materials absorb light, the refractive index, in general, has a non-zero imaginary part. We denote the

complex refractive index by $m(\tilde{\nu}) = n(\tilde{\nu}) + in'(\tilde{\nu})$, where $n(\tilde{\nu})$ is the real part of the refractive index, describing the refractive properties of the material, and $n'(\tilde{\nu})$ is the imaginary part of the refractive index, describing the absorptive properties of the material.

In order to model chemical absorption lines we assume a medium of absorbing dipoles describing both absorption and scattering within the framework of the Lorentz model, briefly reviewed in Appendix A. In the IR spectroscopy the dipoles are the absorbing functional groups. The Lorentz model, providing the complex dielectric constant $\tilde{\varepsilon}_r$ according to Eq. A18, then allows the computation of the complex refractive index *m* via Eq. A20. In principle, even complex biological materials containing many absorbing functional groups are exactly described by Eq. A18. However, in practice a parameterization of the Lorentz model according to Eq. A21 turns out to be very effective. The only input parameters to this effective model are the positions, widths and strength of the absorption bands. Because of the functional form of the effective Lorentz model, the real and the imaginary parts of the complex refractive index *m* automatically fulfil the Kramers-Kronig relation [15, 16].

Mie scattering

A rigorous Mie-type model for scattering of infrared light at cells

The strong Mie-type scattering artifacts, that are often present in FTIR spectra of cells, have so far been approximated using analytical expressions derived from the Mie theory [13, 14, 20]. The extinction cross section $\sigma_{ext}(\tilde{\nu})$ for the scattering of light at a spherical particle is described by the Mie theory [26] and given by

$$\sigma_{ext}(\tilde{\nu}) = \pi a^2 Q_{ext}(\tilde{\nu}), \qquad (9)$$

where *a* is the radius of the scattering particle. Gustav Mie derived the exact solutions of this problem, which are expressed in terms of spherical Bessel functions. The interested reader is referred to the book by Van De Hulst [26]. It has been shown that for the case of $|m - 1| \ll$

1, where m is the complex refractive index, $Q_{ext}(\tilde{\nu})$ can be approximated by the following formula [26]

$$Q_{ext}(\tilde{\nu}) \approx 2 - 4e^{-\varrho \tan\beta}\frac{\cos\beta}{\rho} sin(\rho - \beta) - 4e^{-\varrho \tan\beta}\left(\frac{\cos\beta}{\varrho}\right)^2 cos(\varrho - 2\beta) + 4\left(\frac{\cos\beta}{\varrho}\right)^2 cos(2\beta) \quad (10)$$

with

$$\rho = 4\pi a\tilde{\nu}|m-1| \quad \text{and} \quad \tan\beta = n'/(1-n) \quad (11)$$

In the following study we will use the Van de Hulst approximation, since it provides a handy, analytical solution without noticeable loss of accuracy. All the previous and following considerations are valid by either applying the Van De Hulst approximation or the exact Mie solutions. With the help of either the Van De Hulst formula or the exact Mie solutions, the absorbance can be calculated via the extinction cross section $\sigma_{ext}(\tilde{\nu})$ according to Eqs. 3 and 5. The exact Mie solutions and formula 10 (since they contain n and n') are generally valid even if the complex refractive index m has a non-zero imaginary part. In case of a real refractive index, i.e. when absorption is neglected, the Van De Hulst solutions can be simplified to

$$Q_{ext}(\tilde{\nu}) \approx 2 - \frac{4}{\rho} sin\,\rho + \left(\frac{4}{\varrho}\right)^2 (1 - cos\,\varrho) \quad (12)$$

Several efforts have been made to treat the case of Mie scattering with absorption [14, 20, 21]. Although Eq. 10 represents the approximation formula for the case of a complex refractive index, describing precisely the problem of absorption, it has not yet been applied in the literature in connection with the interpretation and extraction of information from measured data.

The extinction efficiency $Q_{ext}(\tilde{\nu})$, expressed by Eq. 12 with real index of refraction, is usually interpreted as the additive scatter contribution to the absorbance spectrum [11, 13,

20]. This is a very rough estimation as we will show in the following. When expanding the logarithm in Eq. 7 in powers of $Q_{ext}(\tilde{\nu})$, it can be seen that to first order in $Q_{ext}(\tilde{\nu})$ we obtain

$$A \approx \frac{\pi a^2}{G\ ln(10)} Q_{ext}(\tilde{\nu}) \quad (13)$$

This shows that the absorbance and the extinction are only approximately proportional to each other. In order to investigate this further we model one absorption band at 1654 cm^{-1} applying the Lorentz model outlined in Appendix A. This band corresponds to the C=O stretching vibration of the peptide bond in proteins. We choose $\Lambda = 10^4$ cm^{-2}, $\Gamma = 30$ cm^{-1}, and $\bar{\varepsilon}_r = 1.44$. Far away from the absorption band at 1654 cm^{-1} the real part of the refractive index is close to $\sqrt{\bar{\varepsilon}_r} = 1.2$, and changes considerably in the vicinity of the band position. In Figs. 2a and b the approximated absorbance for a complex refractive index, calculated according to Eqs. 10 and 7 is compared with the approximated absorbance for a real refractive index obtained from Eq. 10 and 13, using $\frac{\pi a^2}{G} = 0.05$. The approximated absorbance for a complex refractive index is plotted in red, while the approximated absorbance for a real refractive index is plotted in blue. We see that the maximum value of the absorbance appears at the same shifted position $\tilde{\nu}_{max} = 1648\text{cm}^{-1}$. This shows that the approximation with the real refractive index still reveals the approximation with complex refractive index shifted position of the maximum. This is immediately clear, since the derivative of the approximation with complex refractive index formula and the derivative of the approximated formula with the real refractive index are both proportional to the derivative of $Q_{ext}(\tilde{\nu})$. Moreover, the maximum occurs at wavenumbers at which the derivative with respect to $\tilde{\nu}$ is zero. In the low frequency range (approx. below 2000 cm^{-1}) the two curves in Figs. 2 agree very well, while they differ significantly in the high frequency regime. This observation may be important for fitting spectra of single cells, where so far only the approximated formula with the real refractive index has been used [13, 14, 20, 21].

In addition, we point out that the formulas for $Q_{ext}(\tilde{\nu})$ in Eqs. 10 and 12 are applicable only if the incident light is a plane wave, i.e. the size of the incident beam is infinite and the incoming light rays are parallel. When beam sizes are of the same order as the particle sizes, the computations of $Q_{ext}(\tilde{\nu})$ have to be modified and the expression for $Q_{ext}(\tilde{\nu})$ may change significantly. This also shows that $Q_{ext}(\tilde{\nu})$ can be taken only as a rough approximation for the scattering of infrared light at single cells when using highly focused infrared beams such as in synchrotron infrared spectroscopy. A further investigation of this topic has to show how well $Q_{ext}(\tilde{\nu})$ in Eq. 10 describes the experimental situation [27]. In addition, the incident beam in synchrotron infrared spectroscopy has a high numerical aperture and the condition of parallel light rays is not exactly fulfilled [27].

In order to take the numerical aperture into account when calculating the apparent absorbance, we calculate the light intensity *I* from the exact Mie solutions. Since synchrotron radiation is linearly polarized, the field vector $\vec{E}_0$ of the incident synchrotron light may be decomposed into a component $\vec{E}_{0r}$ perpendicular to the scattering plane and a component $\vec{E}_{0l}$ parallel to the scattering plane. Denoting by φ the (azimuthal) angle between $\vec{E}_0$ and the scattering plane ([26], section 9.3), the magnitudes of the perpendicular and parallel components of $\vec{E}_0$ are given by $E_{0r} = E_0 \sin(\varphi)$ and $E_{0l} = E_0 \cos(\varphi)$, respectively. Taking the detector aperture *G* and the geometrical cross section g into account, the scattered intensities I_r and I_l are given explicitly by ([26], section 4.4)

$$I_r(\theta,\varphi) = \left(\frac{G}{g}\right)\frac{i_1(\theta)}{4\pi^2\tilde{\nu}^2r^2}|E_{0r}|^2 = \left(\frac{G}{g}\right)\frac{i_1(\theta)}{4\pi^2\tilde{\nu}^2r^2}I_0 sin^2(\varphi) \qquad (14)$$

and

$$I_l(\theta,\varphi) = \left(\frac{G}{g}\right)\frac{i_2(\theta)}{4\pi^2\tilde{\nu}^2r^2}|E_{0l}|^2 = \left(\frac{G}{g}\right)\frac{i_2(\theta)}{4\pi^2\tilde{\nu}^2r^2}I_0 cos^2(\varphi) \qquad (15)$$

where $I_0 = |E_0|^2$, r is the distance between sample and detector, $i_{1,2}(\theta) = \left|S_{1,2}(\theta)\right|^2$, and $S_{1,2}(\theta)$ are the scattering amplitudes stated explicitly in Appendix B, Eqs. B1 and B2. In order to account for the numerical aperture, we integrate

$$I(\theta, \varphi) = I_r(\theta, \varphi) + I_l(\theta, \varphi) \quad (16)$$

over the solid angle cone with opening angle θ_{NA} (the aperture angle) to obtain the intensity I_{NA}, corresponding to the given numerical aperture, according to

$$I_{NA} = \int_0^{\theta_{NA}} \int_0^{2\pi} I(\theta, \varphi) \sin(\theta)\, d\theta\, d\varphi = \left(\frac{G}{g}\right) \frac{I_0}{4\pi\tilde{\nu}^2 r^2} \int_0^{\theta_{NA}} [i_1(\theta) + i_2(\theta)] \sin(\theta)\, d\theta. \quad (17)$$

In our simulations we used r = 0.5 m. This turned out to be the optimal value resulting from our calculations and is a reasonable value for our optical setup as well. The parameter G was estimated with the EMSC model. Inserting the transmission $T = I_{NA}/I_0$ into Eq. 5, we obtain the absorbance

$$A = -\log_{10} \left\{ \left(\frac{G}{g}\right) \frac{1}{4\pi\tilde{\nu}^2 r^2} \int_0^{\theta_{NA}} [i_1(\theta) + i_2(\theta)] \sin(\theta)\, d\theta \right\} \quad (18)$$

For the calculation of the exact Mie solutions the algorithm proposed by Bohren and Huffman [28] was implemented in MATLAB.

Iterative algorithm

We will follow the iterative algorithm proposed by van Dijck et al. [1], in order to recover the pure absorbance spectrum A from measured and distorted absorbance spectra $A_{measured}$. The main steps of the algorithm are presented below.

Initialization: For $j = 1$, the complex refractive index $m_j = n_j + i\, n'_j$ is initialized, where j is the index of iteration. The real part of the refractive index, n_j, is initialized with an estimated constant n_0. The imaginary part, n'_j, is initialized with zero.

Following initialization, the iteration proceeds as follows:

I. The formulas in appendix B together with Eq. 18 are used to predict the absorbance spectrum $A^{(j)}$ from the complex refractive index m_j.

II. The difference $E^{(j)}$ between the measured spectrum $A_{measured}$ and the predicted spectrum $A^{(j)}$ is calculated according to:

$$E^{(j)}(\tilde{\nu}) = A_{measured}(\tilde{\nu}) - A^{(j)}(\tilde{\nu}) \qquad (19)$$

III. From the difference and using Eq. C19, the next value for *n'* is calculated according to:

$$n'_{j+1}(\tilde{\nu}) = n'_{j}(\tilde{\nu}) + \frac{\ln(10)}{4\pi\tilde{\nu}d_{eff}} E^{(j)}(\tilde{\nu}), \qquad (20)$$

where $d_{eff} = \frac{4a}{3}$ is the effective thickness of a sphere of radius *a*.

IV. The negative values of $n'(\tilde{\nu})$ are set to zero.

V. A new value for $n\ (\tilde{\nu})$ is predicted according to:

$$n_{j+1}(\tilde{\nu}) = n_0 + Kramers\ Kronig\left[n'_{j+1}(\tilde{\nu})\right] \qquad (21)$$

VI. The new complex refractive index is calculated according to:

$$m_{j+1}(\tilde{\nu}) = n_{j+1}(\tilde{\nu}) + i\ n'_{j+1}(\tilde{\nu}) \qquad (22)$$

The complex refractive index $m_{j+1}(\tilde{\nu})$ is updated and the next iteration with $j + 1$ is started.

Estimation of the radius and the constant part of the real part of the refractive index

In order to estimate the constant part of the refractive index n_0 and the radius of the sphere *a*, intervals of n_0 and *a* may be considered. For every combination of these two parameters we calculate the Q_{ext} with Eq. 12. The absorbance, A_{pred}, is predicted using Eq. 13. The parameter *G* is estimated using EMSC model. For direct comparison of the predicted spectrum with the spectrum measured at the discrete wavenumbers $\tilde{\nu}_i$, we suggest to calculate the root mean square error (RMSE) according to

$$E^{(j)}(\tilde{\nu}_i) = A_{measured}(\tilde{\nu}_i) - A_{pred}(\tilde{\nu}_i) \qquad (23)$$

$$RMSE^{(j)} = \sqrt{\frac{\sum_{i=1}^{K}\left[E^{(j)}(\tilde{\nu}_i)\right]^2}{K}} \qquad (24)$$

where K is the number of measured discrete wavenumbers $\tilde{\nu}_i$. The iterative algorithm described in the previous section is very time-consuming when full Mie theory is applied and the integration over the numerical aperture is executed. Therefore, we suggest to use the van de Hulst approximation formula in Eq. 12 in order to obtain a first estimate of n_0 and a. This result can then be entered into the iterative algorithm using the full Mie theory and integrating over the numerical aperture. Since the van de Hulst approximation formula in Eq. 12 depends on the size factor

$$\alpha = a(n_0 - 1). \qquad (25)$$

and not on n_0 and a, separately, it is sufficient to minimize the RMSE as a function of α. Thus, this first estimate results only in an estimate of α, but not in an estimate of n_0 and a, separately. We emphasize that the size factor α needs to be carefully distinguished from the size parameter $x = k \cdot a$ and from the parameter $\rho = 2x|m - 1|$, defined in Eq. 11.

3. Experiment

Samples of pollen were collected at the Botanical Garden of the Faculty of Science of the University of Zagreb during the 2012 pollination season. The following samples, belonging to the *Cupressaceae* plant family, were measured: *Cunninghamia lanceolata*, *Juniperus chinensis*, *Juniperus communis*, and *Juniperus excels*. The pollen samples, of approximately spherical morphology, varied in diameter between 10 to 40 μm. The samples were collected directly from plants at flowering time by shaking mature male cones. The samples were kept

in paper bags at room temperature for 24 hours, and afterwards transferred to vials and stored at -15 °C.

In addition to the pollen samples, polymethyl methacrylate (PMMA) microspheres of assorted sizes were measured as well as a simple artificial system for modeling scattering from biological materials. The PMMA samples were purchased from Microspheres-Nanospheres (Corpuscular Inc, NY), and used without further modifications. The spheres had the following diameters as stated by the vendor: 5.5, 10.8, 15.7, 20.0, 30.0 and 40.0 µm.

In order to obtain high-quality spectra of single particles, pollen and PMMA samples were recorded by using synchrotron radiation at the SOLEIL synchrotron facility. The synchrotron spectra were measured on the SMIS infrared beamline, details of which can be found elsewhere [29]. The transmission spectra of all the samples were recorded with a resolution of 4 cm^{-1} by using the synchrotron radiation coupled to a Nicolet 5700 FTIR spectrometer with a Nicolet Continuum XL IR microscope (Thermo Scientific, CA), equipped with a liquid nitrogen cooled mercury cadmium telluride detector. The spectra were measured in the 8000-650 cm^{-1} spectral range, with 128 scans each and using 15× and 32× objectives with different aperture sizes, depending on the size of the sample (10x10µm, 15x15µm and 20x20µm). The numerical aperture of the microscope was 0.65 [29]. For each measured sample an image was recorded with an optical microscope.

4. Results and Discussion

Comparison with existing Mie-type models for cells

In the literature, the extinction $Q_{ext}(\tilde{\nu})$ in Eq. 12, i.e. the Van De Hulst approximation for a real refractive index, has frequently been used as an approximation for the absorbance [13, 14,

20, 21]. In the paper by Bassan et al. [14], Mie scattering in the infrared spectroscopy of single cells is constructed theoretically, taking the chemical absorption of the scatterer into account. The case where absorption is considered was termed resonant Mie scattering. Starting from a practically scatter-free thin-film absorbance spectrum *A*, the imaginary part of the complex index of refraction, *n'*, is calculated, assuming proportionality between *n'* and *A*. Because of the explicit frequency dependence, as discussed in [1] (see Eq. 8), this is only approximately valid. After determining *n'*, a Kramers-Kronig transformation [15, 16] according to

$$n(\tilde{\nu}) = n_0 + \frac{2}{\pi} P \int_0^{\infty} \frac{s \cdot n'(s)}{s^2 - \tilde{\nu}^2} ds \qquad (26)$$

is applied to obtain the real part of the index of refraction *m*. At this point the real part is inserted into Eq. 12 in order to obtain the extinction efficiency $Q_{ext}(\tilde{\nu})$. It is important to note that this involves neglecting the imaginary part of the refractive index *m*, since Eq. 10 is equivalent to Eq. 12 only if the index of refraction is real. The result obtained was called apparent absorbance [14]. The approximation involved in calculating the apparent absorbance is not negligible, as we will see in the following. In Figs. 3a and 3b, using the same model absorption line as in Fig. 2 at 1654 cm^{-1}, the apparent absorbance with real refractive index is plotted in blue, while the apparent absorbance result, obtained via Eqs. 3, 4 and 10, employing the complex refractive index, is plotted in red. It can be seen that the apparent absorbance is shifted to lower frequencies compared to the result with complex index of refraction. The apparent absorbance has a shifted maximum at $\tilde{\nu}_{max} = 1641\mathrm{cm}^{-1}$, which corresponds to a low-wavenumber shift of 7 wavenumbers with respect to its expected location at $\tilde{\nu}_{max} = 1648\mathrm{cm}^{-1}$ (see Fig. 2), a significant difference when interpreting spectral bands of biological materials. Concerning the system at hand, we have found that the shift is to the right (lower wavenumber region) if the band is located on the right wing of the associated Mie fringe, and the shift is to the left (higher wavenumber region) if the band is located on the left-hand side

of the associated Mie fringe. While this observation applies to our model and our current choice of parameters, it is an open question whether shift directions and band locations are correlated this way in general.

A Mie-type model for a nucleus in a cell membrane

It is important to note that the approximation expression with complex index of refraction for the extinction efficiency $Q_{ext}(\tilde{\nu})$ (for the approximate version with real index of refraction see Eq. 10) takes absorption and scattering into account and thus it is expected that this expression can be used to obtain an expression for the absorbance of infrared light by a cell nucleus. However, if the nucleus is embedded in a medium, the absorbance of the cell plasma may add to the absorbance of the nucleus obtained via Eqs. 3, 4 and 10. In this case the absorbance spectrum for the nucleus $A_{nucleus}$ can be obtained according to Eqs. 3, 4 and 10, considering the nucleus as a scattering and absorbing sphere. The absorbance spectrum of the plasma A_{plasma} may be a relatively undistorted spectrum, since the plasma can be considered as a thin film, in which the nucleus is embedded. The measured spectrum $A_{measured}$ may therefore be simply written as the sum of the two contributions according to

$$A_{measured} = A_{nucleus} + A_{plasma} \quad (27)$$

The above findings may be used to improve the algorithm of Refs. [20, 21], which employs the model constructed by Bassan et al. [14].

Ripples

The exact Mie extinction shows a rapidly fluctuating structure on top of the smooth wavelike underlying structure. The sharp narrow structures are called ripples, while the broader, smoother structures are called wiggles. The wiggles are always present in the extinction curve and if we increase the size factor, ripples start to appear on top of wiggles. We modelled an absorbance band at 1654 cm^{-1} using the Lorentz model presented in Appendix A. We calculated the Mie extinction, Q_{ext}, and the scattering efficiency, Q_{sca} using the exact Mie

solutions (see Appendix B equations B3, B4, B7 and Eqs. 15-16) and the modelled complex index of refraction, according to the following equations:

$$Q_{ext} = \frac{2}{x^2}\sum_{n=1}^{\infty}(2n+1)\Re(a_n + b_n) \quad (28)$$

$$Q_{sca} = \frac{1}{x^2}\int_0^{\theta_{NA}}[i_1(\theta) + i_2(\theta)]\sin\theta\, d\theta. \quad (29)$$

In Fig. 4 we plot the exact Mie extinction, Q_{ext}, and the scattering efficiency, Q_{sca}, for an absorbing sphere, for two cases, n_0=1.14, a=10μm and n_0=1.24, a=10μm. In Fig. 4a, the case of n_0=1.14, a=10μm, we see only the large oscillations (wiggles) in Q_{ext} and Q_{sca}. In Fig. 4b, we see the ripples in Q_{ext} and Q_{sca} when n_0=1.24, a=10μm. The formal reason for the ripples in the Mie absorbance spectra is known: they correspond to partial-wave resonances in the Mie coefficients [30, 31]. However, the excitation mechanisms of these resonances and their consequences for the electromagnetic field distribution inside the scatterer have not been explored yet.

The synchrotron FTIR spectrum of a PMMA sphere with 10 μm diameter is shown in Fig. 5a. In Figs. 5b and 5c, the spectrum has been divided into 1) the spectral region 7200-3600 cm^{-1} and 2) the spectral region 3600-800 cm^{-1} respectively. While the spectrum in Fig. 5b shows only features caused by the Mie scattering of the sphere, the spectrum in Fig. 5c shows the additional features due to absorbance of the PMMA molecules. Zooming into the wavenumber region between about 6000 cm^{-1} and 7000 cm^{-1} (see Fig. 5d), we see sharp structures in the absorbance that may correspond to Mie ripples. To our knowledge, the observation of Mie ripples was not yet reported in the experimental FTIR literature. Thus, the features in Fig. 5d may constitute the first experimental observation of Mie ripples in an FTIR spectrum. Since the present paper does not focus on the ripple structure, but focuses instead on the extraction of pure absorbance spectra, we defer the discussion of ripples in absorbance spectra to a forthcoming paper.

Recovery of pure absorbance spectra of PMMA spheres

In order to test the algorithms, we used PMMA spheres as a model system. The value of the constant part of refractive index, n_0, for PMMA spheres is known approximately and thus a good estimate for the radius of the spheres, a, can be obtained. We used the measured spectrum from Fig. 5b to test the prediction method for the radius of the sphere and the constant part of the refractive index as described in the theory section. We considered the following intervals for n_0 and for a (radius of the sphere):

$$n_0 \in [1.1; 2.0]\, \Delta n_0 = 0.05$$

$$a \in [1\mu m; 10\mu m] \quad \Delta a = 0.25\mu m$$

We calculated the RMSE as a function of α. The result is shown in Fig. 6, where RMSE is plotted as a function of $\alpha \cdot 10^6$. We will refer to α as the size factor, as frequently done in the literature. We find four major local minima in the RMSE function: at α=0.64μm, α=1.1μm, α=2.1μm and α=3.1μm (see inset of Fig. 6). The global minimum is located at approximately α=2.1μm. Figure 7 shows the predicted absorbance, calculated with Eqs. 12-13, together with the measured absorbance, for all four local minima. The best fit to the large oscillation in the measured absorbance spectrum in Fig. 5b is found for $\alpha = 2.1\mu m$. We consider the value 2.1μm a good solution. In the case of PMMA we know that the approximate value of n_0 is 1.48. Considering the minimum in the RMSE function around α=2.1μm, we obtain the radius $a = \frac{\alpha}{n_0 - 1} = 4.4$ μm.

In our case we know the radius of the PMMA sphere and this helps to choose the correct n_0. But if we do not have information about the radius or the refractive index, we can choose a and n_0 values which satisfy the α=2.1μm condition. We will use these values (n_0 and a) as initial parameters in the van Dijck iterative algorithm. If we can recover the pure absorbance spectra and if we have a good predicted absorbance, then the initial parameters are a good

choice. If we cannot recover the imaginary part of the refractive index, or the predicted absorbance is not good, we discard the n_0 and a combination.

Consider the measured spectrum in Fig. 5c. To test our initial parameters, n_0=1.48 and a=4.4μm, we selected three different combinations of n_0 and a as inputs for the the van Dijck iterative algorithm, i.e. (i) n_0=1.7 and a=3μm, (ii) n_0=1.48 and a=4.4μm and (iii) n_0=1.3 and a=7μm. Following the choice of n_0, all three values of a were obtained via $a = \frac{2.1\ \mu m}{n_0 - 1}$. The n_0 values were chosen such that the resulting a values box in and thereby test our initial parameter set n_0=1.48 and a=4.4μm. Running the van Dijck iterative algorithm for the three selected values of n_0 and a, we predicted our apparent absorbance using the exact Mie solutions from Eq. 18. This way we take into account the numerical aperture. After 12 iteration steps the algorithm converged and the imaginary part, n', of the refractive index and the predicted absorbance was obtained (Figures 8-9 respectively). As can be seen in Fig. 9, the predicted absorbance, for the values n_0=1.7 and a=3μm does not provide a good fit. The solution n_0=1.3 and a=7μm provides a better fit both for the imaginary part and the predicted absorbance. The best combination is n_0=1.48 and a=4.4μm, as both the imaginary part of the refractive index and the predicted absorbance agree best. With this obtained n' we calculate the pure absorbance spectrum of a PMMA thin film and consider the thickness to be $d_{eff} = \frac{4a}{3} = 5.9\mu m$:

$$A_{pure} = \frac{4\pi n' d_{eff} \tilde{\nu}}{ln(10)} \qquad (30)$$

Figure 10 shows this calculated pure absorbance spectrum of a PMMA thin film computed with Eq. 30. The main absorbance peaks in the calculated spectrum are compared with other experimental measurements. The following bands were found in the calculated absorbance spectrum: 2987 cm^{-1}, 2937 cm^{-1}, 2839 cm^{-1}, 1763 cm^{-1}, 1724 cm^{-1}, 1497 cm^{-1}, 1466 cm^{-}, 1441 cm^{-1}, 1394 cm^{-1}, 1333 cm^{-1}, 1261 cm^{-1}, 1225 cm^{-1}, 1182 cm^{-1}, 1047 cm^{-1} and 951 cm^{-1}. The

FTIR spectra of PMMA powder have been measured in the range of 4000 – 400 cm^{-1} by Haris et al. The following characteristic absorption bands were found: 3000 cm^{-1}, 2953 cm^{-1}, 2840 cm^{-1}, 1727 cm^{-1}, 1483 cm^{-1}, 1447 cm^{-1}, 1437 cm^{-1}, 1398 cm^{-1}, 1367 cm^{-1}, 1267 cm^{-1}, 1239 cm^{-1}, 1197 cm^{-1}, 1147 cm^{-1}, 1050 cm^{-1}, 990 cm^{-1}, 967 cm^{-1}, 913 cm^{-1}, 840 cm^{-1}, 807 cm^{-1} and 750 cm^{-1} [32]. Our calculated absorbance is in good agreement with the experimental data. With this method it was possible to get the pure absorbance spectra and to give a realistic estimate of n_0 and a. The method will now be tested on biological systems.

Recovery of pure absorbance spectra of Pollen

Pollen grains are an ideal real-world model system for characterization of scattering phenomena of biological samples. As opposed to the vast majority of cells and tissues that are easily deformed, pollen grains have stable and reproducible morphology because of their thick and shape-persistent grain walls. Moreover, the desiccated nature of the grains provides relatively stable biochemical composition, and thus enables simple manipulation and measurement. Finally, the diversity of pollen morphologies, with a variety of shapes, textures, and sizes (ranging from less than 5 μm to over 200 μm), enable a wide range of experimental conditions for the measurement of scattering phenomena.

Pollen grains belonging to the *Cupressaceae* plant family were chosen due to their approximately spherical shape and appropriate range of radius sizes. The synchrotron spectrum of *Juniperus chinensis* pollen grain, with 27 μm diameter, is shown in Fig. 11a. In Fig. 11a we can distinguish three main parts of the spectrum. The first part, between 6300-3600 cm^{-1}, is shown in Fig. 11b. The second part, between 3600-1000 cm^{-1}, is plotted in Fig. 11c. In Fig. 11b we can see the large oscillations due to Mie scattering. In this interval Mie scattering is the main physical origin of the spectrum. Figure 11c shows the absorption part of

the spectrum. In this area the molecular absorption is very strong and together with the scattering is causing an FTIR spectrum. If we zoom into Fig. 11c, we see that for wavenumbers between 2771-1880 cm^{-1}, absorption is not present and Mie scattering is again the guiding phenomenon. Figure 11d shows this zoomed-in spectrum. Within this region the chemical constituents of pollen do not show any absorbance. Thus, in this region *n'* is zero.

In all the spectral regions shown in Fig. 11, we can see the ripples caused by Mie scattering. To the best of our knowledge, this is the first time that Mie scattering ripples were observed in IR spectra of a biological system. As stated before, we do not focus on them in this paper. Our main purpose here is to recover the pure absorbance spectra of the pollen and make a good guess concerning the refractive index and the radius of the pollen grains. In order to achieve this, we use the scenario developed for the PMMA spheres. We will consider the spectrum from Fig. 11b as a measured absorbance and we will try to predict the radius of the pollen grain, a, and the constant part of the refractive index, n_0. The following intervals were chosen for n_0 and for a:

$$n_0 \in [1.1; 2.0]\ \Delta n_0 = 0.05$$

$$a \in [5\mu m; 15\mu m] \quad \Delta a = 0.25\mu m$$

For every combination of these two parameters we predicted the absorbance spectrum with the van de Hulst approximation formula from Eq. 12. We scaled the prediction with EMSC and compared with the measured spectrum. We calculated the root mean square error (RMSE) function according to Eqs. 23-24. The same investigation is followed as in the case of PMMA: In Fig. 12 the resulting RSME function is plotted as a function of the size factor, clearly revealing four distinct minima at α=1μm, α=1.3μm, α=2.2μm and α=3.2μm (see inset of Fig. 12). Figure 13 shows the predicted absorbance for some selected values of the size factor. All combinations of n_0 and a around the parameter value $\alpha = 2.2\mu m$ give a good approximation to the large oscillation in the measured absorbance spectrum, and therefore we

consider the value 2.2 as the best solution. We took this value as the guiding value. From the optical image of the pollen grain we estimated the radius of the pollen grain, a=13.5µm. Choosing the size factor 2.2 for the constant part of the refractive index, we get n_0=1.16. Considering that all the biological materials inside the pollen grain (cellulose, sporopollenin, etc.) have a constant part of the index of refraction of about 1.5 in the visible spectrum of light, this value is quite small. However, taking the porous structure of the outer part of the pollen grain into account, this value makes sense. Therefore, from biological point of view the smaller value of n_0 is the better choice.

We fed different values of n_0 and a as initial parameters into the van Dijck iterative algorithm. If the pure absorbance spectrum is recovered, and if we get a good predicted absorbance, then the initial parameters were a good choice. If the imaginary part of the refractive index is not recovered, or the predicted absorbance is not good, the corresponding combination of n_0 and a was discarded.

Before running the iterative algorithm we tested the prediction method suggested by van Dijck et al.. To predict n_0, these authors propose to use the region from the measured spectrum between 2600 cm^{-1} and 2100 cm^{-1}, as here most organic materials do not show absorption. In the case of *Juniperus chinensis* pollen grains we used the region of the spectrum between 2771 cm^{-1} and 1880 cm^{-1}, shown in Fig. 13c, to predict a and n_0. If we use the same method presented above, with the same interval and resolution of n_0 and a, we obtain for the RMSE function the values plotted in Fig. 14. Employing our prediction method only in this region results a size factor around 3.2. We conclude that in our case the region recommended by van Dijck et al. is not enough to predict n_0 and a.

We continue with our investigation to obtain the pure absorbance spectrum of the pollen grain in the following way. We considered the measured spectrum shown in Fig. 11c. Then, we ran the van Dijck iterative algorithm for two values of n_0 and a (n_0=1.16,

a=13.5µm; n_0=1.5, a=13.5µm). Using the iterative process, we predicted the apparent absorbance using the exact Mie solutions according to Eq. 18 taking into account the numerical aperture. In the region from 2771 cm^{-1} to 1880 cm^{-1} *n'* is kept zero. The imaginary part, *n'*, of the refractive index and the predicted absorbance converged after 20 iteration steps in each case. Figures 15-16 show the imaginary part of the refractive index and the predicted absorbance, respectively. For n_0=1.16, a=13.5µm, the imaginary part of the refractive index shows vibrational bands at the expected positions. Yet, the obtained imaginary part of the refractive index does not resemble a scatter-free pollen spectrum. Especially the region from 1800 cm^{-1} to 1000 cm^{-1} shows an unexpected signature. In case of n_0=1.5, a=13.5µm no meaningful peaks in imaginary part could be reconstructed as can be seen in Fig. 15.

The predicted spectrum obtained for the case n_0=1.16, a=13.5µm represents a meaningful prediction. The regions with absorption bands were nicely predicted. The case n_0=1.5, a=13.5µm does not reveal a meaningful prediction.

5. Conclusions

In recent years, infrared spectroscopy of biological materials has been challenged by samples of increasing morphological complexity, with the consequence that infrared spectra are strongly distorted by scattering. Several efforts have been made to explain the observed scattering phenomena, and approximate models for the different situations have been presented. All the models presented so far are ad hoc models. In this paper we have presented an exact description of the absorbance spectrum for the scattering and absorption of infrared light at spheres of absorbing materials.

When dealing with Mie scattering, absorption and scattering cannot be treated as independent. In this paper we have shown that current models that treat absorption and scattering as dependent yield approximate absorption bands that are considerably shifted, as opposed to the

exact models presented in this paper. We therefore propose to implement the exact models in the existing EMSC algorithms for reconstructing absorbance spectra. Concerning the Mie formalism, both the approximate, analytical or the exact Mie formulas [26] may be used.

Our method for the estimation of n_0 and a works well in the case of homogeneous spheres, but may be too simple in the case of pollen. It may be necessary to take the layered structure of the pollen into account.

The pure absorbance spectra were successfully recovered for PMMA spheres. For biological systems no satisfactory recovery of the pure absorbance spectrum could be obtained. As we demonstrated in this paper, good starting values for n_0 may often be obtained on the basis of physical and biological considerations. Using these values of n_0 as starting values, pure absorbance spectra can be obtained with a high level of confidence. Motivated by the need of accurate n_0 values, we are currently developing new methods of extracting n_0 from the scattering data themselves. Combining these new methods for determining n_0 with the methods outlined and demonstrated above brings out the full power of the new techniques advanced in this paper and contributes decisively to the solution of extracting pure absorbance spectra from measured FTIR spectra.

Appendix A: Lorentz Model

The Lorentz model is a classical model for the computation of the dielectric constant of a material in the presence of absorption resonances. Although based on classical electrodynamics, including quantum effects only phenomenologically via the (measured) spectrum of discrete molecular frequencies, it is surprisingly effective in explaining the frequency dependence of the complex index of refraction m. In particular, it correctly predicts the Lorentz-type shape of the imaginary part of m, which closely resembles the line shape of an absorption resonance. For the derivation of the Lorentz model, we follow the excellent presentations by Griffiths [33] and Parson [34]. The Lorentz model in its simplest form assumes that an electron is bound to an atom or molecule with a harmonic binding force

$$F_b = -M\omega_0^2 x \quad \text{(A1)}$$

where M is the mass of the electron, ω_0 is the natural oscillation frequency of the electron in the harmonic binding potential and x is the amplitude of vibration of the electron in the direction of the external electric field $\vec{E}$ which, in our case, is the infrared light field. It is not necessary to restrict ourselves to electrons. Any charged particle or active group of charged particles that may execute a vibration, such as, e.g., O-H or C=O stretches, are successfully described by the Lorentz model. Therefore, from now on, we imagine a "particle" with effective mass M and charge q subject to the binding force in Eq. A1, and substitute "electron", or "chemically active group" for "particle", as the case may be. For electrons, for instance, $q = -e$, where $e = 1.602 \times 10^{-19}$ C is the elementary charge. For chemically active groups, q is substituted with the polarization charge δq of the polar ends of the group. When the particle vibrates, it loses energy, for instance by electromagnetic dipole radiation or by energy transfer to the backbone molecule or the medium, via the long-range Coulomb force. We model this energy loss with a damping force

$$F_\gamma = -M\gamma \frac{dx}{dt} \quad \text{(A2)}$$

which depends linearly on the speed $\frac{dx}{dt}$ of the vibrating particle, and γ is the damping constant, which depends on the details of the energy dissipation processes. In addition to the binding force F_b and the damping force F_γ, the particle also experiences the driving force

$$F_d = qE(t) + \frac{qP(t)}{3\varepsilon_0} \quad \text{(A3)}$$

where

$$E(t) = E_0 \cos \omega t \quad \text{(A4)}$$

is the field strength of the infrared light as a function of time , ω is its frequency and

$$P(t) = Nqx(t) \quad \text{(A5)}$$

is the polarization induced by the external field and N is the number of particles per unit volume. We assume here a linear dielectric, in which the polarization of the medium is directly proportional to the radiation field. Newton's equation of motion for the particle,

$$M\frac{d^2x}{dt^2} = F_b + F_\gamma + F_d \quad \text{(A6)}$$

leads to the differential equation

$$M\frac{d^2x}{dt^2} + M\gamma\frac{dx}{dt} + M\omega_0^2 x = qE_0\cos\omega t + \frac{qP(t)}{3\varepsilon_0} \quad \text{(A7)}$$

for the position of the particle. The solution of Eq. A7 is greatly simplified if we consider Eq. A7 as the real part of the complex equation

$$\frac{d^2\tilde{x}}{dt^2} + \gamma\frac{d\tilde{x}}{dt} + \omega_0^2\tilde{x} = \frac{q}{M}\tilde{E} + \frac{q}{3\varepsilon_0 M}\tilde{P} \qquad \text{(A8)}$$

where x is the real part of the complex quantity $\tilde{x}$,

$$\tilde{E} = E_0 e^{-i\omega t} \quad \text{(A9)}$$

is the complex electric field and

$$\tilde{P} = Nq\tilde{x} \qquad \text{(A10)}$$

is the complex polarization. In infrared spectroscopy we are not interested in the transient solutions of Eq. A8, i.e. solutions which are generated by switch-on and switch-off of the infrared light. These solutions quickly decay exponentially in time. Once the transient solutions have decayed, the system settles into the steady-state solution

$$\tilde{x} = \tilde{x}_0 e^{-i\omega t} \quad \text{(A11)}$$

Inserting this into Eq. A8 and using Eq. A10, we obtain

$$\tilde{x}_0 = \frac{q/M}{\omega_0^2 - \omega^2 - \frac{q^2 N}{3\varepsilon_0 M} - i\gamma\omega} E_0 \qquad \text{(A12)}$$

The complex dipole moment of the particle is

$$\tilde{p} = q\tilde{x} = \frac{q/M}{\omega_0^2 - \omega^2 - \frac{q^2 N}{3\varepsilon_0 M} - i\gamma\omega}\tilde{E} \quad \text{(A13)}$$

We now assume that we have N_m active molecules in our sample and each molecule consists of f_s particles with masses M_s, charges q_s, resonance frequencies ω_s and damping constants γ_s. We define

$$\Omega_s^2 = (\omega_s)^2 - \left(\frac{q_s^2 N_m}{3\varepsilon_0 M_s}\right) f_s \qquad \text{(A14)}$$

The polarization $\tilde{P}$, i.e. the dipole moment per unit volume, is given by

$$\tilde{P} = \varepsilon_0\tilde{\chi}\tilde{E} \qquad \text{(A15)}$$

where ε_0 is the permittivity of the vacuum,

$$\tilde{\chi} = N_m \sum_s \frac{q_s^2 f_s/M_s}{\Omega_s^2 - \omega^2 - i\gamma_s\omega} \quad \text{(A16)}$$

is the susceptibility and $\tilde{E}$ is the complex electric field defined in Eq. A9. The dielectric constant is

$$\tilde{\varepsilon} = \varepsilon_0 \tilde{\varepsilon}_r \qquad \text{(A17)}$$

where the relative dielectric constant $\tilde{\varepsilon}_r$ depends on $\tilde{\chi}$ according to

$$\tilde{\varepsilon}_r = 1 + \tilde{\chi} \qquad \text{(A18)}$$

In Eq. A16 we have to sum over all resonances over the entire electromagnetic spectrum including the radio frequency region below the infrared frequency range, the infrared frequency region, and the spectral region above the infrared. We are interested in the infrared frequency region. Therefore, for frequencies larger than infrared frequencies, e.g. in the visible and UV, we may neglect $\gamma_s \omega$ with respect to ω^2 and Ω_s^2, and expand Eq. A16 to first order in $\left(\frac{\omega}{\Omega_s}\right)^2$. As a consequence, the summation in this frequency range contributes approximately a real term

$$\alpha(\omega) = N_m \sum_k \frac{q_k^2 f_k / M_k}{\Omega_k^2} \left[1 + \left(\frac{\omega}{\Omega_k}\right)^2\right] \qquad \text{(A19)}$$

to the susceptibility in Eq. A16, where the sum over *k* in Eq. A19 extends over all resonances with frequencies above the infrared range. In the case of the resonances below the infrared frequency range, i.e. the far infrared region and radio frequency region, we may neglect Ω_s^2 and $\gamma_s \omega$ with respect to ω^2. Thus, this frequency range, approximately, contributes the frequency dependent term

$$\beta(\omega) = -\frac{N_m}{\omega^2} \sum_l \frac{q_l^2 f_l}{M_l} \qquad \text{(A20)}$$

to the susceptibility in Eq. A16, where the sum over *l* in Eq. A20 is over all the resonances below the infrared frequency range. Thus, all together, we now obtain

$$\tilde{\varepsilon}_r = \bar{\varepsilon}_r + N_m \sum_{s\,\epsilon\,IR} \frac{q_s^2 f_s / M_s}{\Omega_s^2 - \omega^2 - i\gamma_s \omega} \qquad \text{(A21)}$$

where the sum in Eq. A21 extends only over the infrared (IR) resonances and

$$\bar{\varepsilon}_r = 1 + \alpha(\omega) + \beta(\omega) \qquad \text{(A22)}$$

is the frequency dependent effective relative dielectric constant of the medium, i.e. the background dielectric constant, on which the infrared resonances are built. The complex index of refraction is now given by

$$m = \sqrt{\tilde{\varepsilon}_r} \qquad \text{(A23)}$$

At this point two important comments are in order: (1) In optics we are familiar with the phenomenon of dispersion, i.e. the change of the index of refraction with increasing wavelength. For glass, for instance, we know that the index of refraction decreases with increasing wavelength, which gives rise to the familiar observation of the splitting of white light into its constituent colours with the help of a prism. This decrease in the index of refraction is now easily explained. According to Eqs. 19 and 20, both $\alpha(\omega)$ and $\beta(\omega)$ cause a decrease in $\bar{\varepsilon}_r$, and therefore, according to Eq. A23, they also cause a decrease in m, when the wavelength increases. Therefore the Lorentz model explains this basic observation. (2) Since the quantities N_m, q_s , f_s, and γ_s are usually not readily available, we write

$$\tilde{\varepsilon}_r = \bar{\varepsilon}_r + \sum_{s\,\epsilon\,IR} \frac{\Lambda_s}{\tilde{V}_s^2 - \tilde{\nu}^2 - i\Gamma_s\tilde{\nu}} \qquad \text{(A24)}$$

where $\bar{\varepsilon}_r$, $\tilde{V}_s$, Λ_s, and Γ_s are adjustable parameters and

$$\tilde{\nu} = \frac{1}{\lambda} = \frac{\omega}{2\pi c} \qquad \text{(A25)}$$

where λ is the wavelength and c is the vacuum speed of light. This is the microscopic basis for the usual practice in spectroscopy of fitting Lorentzian lines to resonance structures in the index of refraction.

Instead of using quantum mechanics to solve for the quantized excitations of the molecule in the presence of the infrared radiation field, the Lorentz model uses classical mechanics to solve the forced, damped harmonic oscillator equation (A8). This, apparently, introduces two errors, (i) the oscillator (A8) is not quantized and (ii) neither is the radiation field, i.e. it is not treated as consisting of photons. The question is: how serious are these approximations? The answer is the following. (i) Quantum mechanics has been partially included by providing the Lorentz model with the discrete set of molecular frequencies Ω_s, a direct result of the quantization of the molecule via the many-body Schrödinger equation. (ii) Although the radiation field consists of photons, the light intensities in infrared spectroscopy are so high that we can safely neglect the quantization of the radiation field. Of course there remains the question of the quantization of the Ω_s modes, whose amplitudes are treated as a classical, continuous variable, although, according to quantum mechanics, they should be quantized.

This, however, is not serious. As soon as the Ω_s oscillators are appreciably excited, corresponding to a few absorbed photons, the classical approximation is practically indistinguishable from the exact quantum treatment, which is due to the Bosonic nature of the oscillator excitations. Thus, because of the relatively large intensities of the infrared light field, the classical approximation of both the molecular oscillators and the radiation field is justified.

Appendix B: Mie Formulas

The Mie scattering amplitudes are defined as:

$$S_1(\theta) = \sum_{n=1}^{\infty} \frac{2n+1}{n(n+1)} \{a_n \pi_n(cos\theta) + b_n \tau_n(cos\theta)\} \quad \text{(B1)}$$

$$S_2(\theta) = \sum_{n=1}^{\infty} \frac{2n+1}{n(n+1)} \{b_n \pi_n(cos\theta) + a_n \tau_n(cos\theta)\} \quad \text{(B2)}$$

$$a_n = \frac{\psi_n'(y)\psi_n(x) - m\psi_n(y)\psi_n'(x)}{\psi_n'(y)\zeta_n(x) - m\psi_n(y)\zeta_n'(x)} \quad \text{(B3)}$$

$$b_n = \frac{m\psi_n'(y)\psi_n(x) - \psi_n(y)\psi_n'(x)}{m\psi_n'(y)\zeta_n(x) - \psi_n(y)\zeta_n'(x)} \quad \text{(B4)}$$

$$\psi_n(z) = \sqrt{\frac{\pi z}{2}} J_{n+\frac{1}{2}}(z) \quad \text{(B5)}$$

$$\zeta_n(z) = \sqrt{\frac{\pi z}{2}} H^{(2)}_{n+\frac{1}{2}}(z) \quad \text{(B6)}$$

$$x = 2\pi a \tilde{\nu} \quad \text{(B7)}$$

$$y = mx \quad \text{(B8)}$$

$$m = n + in' \quad \text{(B9)}$$

$$\pi_n(cos\theta) = \frac{1}{sin\theta} P_n^1(cos\theta) \quad \text{(B10)}$$

$$\tau_n = \frac{d}{d\theta} P_n^1(cos\theta) \qquad \text{(B11)}$$

where, m (complex in general) is the refractive index of the homogenous sphere, a is the radius of the sphere, J is the Bessel function of the 1st kind and $H^{(2)}$ denotes the Hankel functions. The argument z in Eqs. B5 and B6 is an arbitrary complex number; it may be equal to x or y. P^1 denotes the first order associated Legendre polynomial.

The purpose of listing these equations is twofold: It establishes our notation and shows that all aspects of Mie scattering may indeed be written down analytically. In this context we mention that m in this paper is defined according to B9, with negative n' for positive absorbance. This is the opposite sign convention from the one used in the standard reference book of Van De Hulst [26].

Acknowledgments

The research was supported by the Norwegian Research Council (ISP project Nº. 216687), by the SOLEIL, French national synchrotron facility (project Nº. 20120345), and by the European Commission through the Seventh Framework Programme (FP7-PEOPLE-2012-IEF project Nº. 328289). We thank Paul Dumas and Christophe Sandt from the SMIS beamline at SOLEIL.

References

[1] T. van Dijk, D. Mayerich, P. S. Carney and R. Bhargava, Appl Spectrosc **67** (5), 546-552 (2013).

[2] M. Jackson and H. H. Mantsch, TrAC, Trends Anal. Chem. **11** (6), 206-210 (1992).

[3] J. D. Krusejarres and G. Janatsch, Clinical Chemistry **33** (6), 961-961 (1987).

[4] D. Naumann, D. Helm and H. Labischinski, Nature **351** (6321), 81-82 (1991).

[5] D. L. Wetzel and J. A. Reffner, Cereal Food World **38**, 9-20 (1993).

[6] J. Pijanka, G. D. Sockalingum, A. Kohler, Y. Yang, F. Draux, G. Parkes, K. P. Lam, D. Collins, P. Dumas, C. Sandt, D. G. van Pittius, G. Douce, M. Manfait, V. Untereiner and J. Sule-Suso, Laboratory Investigation **90** (5), 797-807 (2010).

[7] J. K. Pijanka, N. Stone, G. Cinque, Y. Yang, A. Kohler, K. Wehbe, M. Frogley, G. Parkes, J. Parkes, P. Dumas, C. Sandt, D. G. van Pittius, G. Douce, G. D. Sockalingum and J. Sule-Suso, Spectroscopy-an International Journal **24** (1-2), 73-78 (2010).

[8] P. Lasch, A. Pacifico and M. Diem, Biopolymers **67** (4-5), 335-338 (2002).

[9] M. C. McCann, M. Hammouri, R. Wilson, P. Belton and K. Roberts, Plant Physiol. **100** (4), 1940-1947 (1992).

[10] A. Kohler, C. Kirschner, A. Oust and H. Martens, Appl. Spectrosc. **59** (6), 707--716 (2005).

[11] B. Mohlenhoff, M. Romeo, B. R. Wood and M. Diem, Biophys. J. **88** (5), 3635–3640 (2005).

[12] G. Mie, Annalen der Physik **25** (1908).

[13] A. Kohler, J. Sule-Suso, G. D. Sockalingum, M. Tobin, F. Bahrami, Y. Yang, J. Pijanka, P. Dumas, M. Cotte, D. G. van Pittius, G. Parkes and H. Martens, Appl Spectrosc **62** (3), 259-266 (2008).

[14] P. Bassan, H. J. Byrne, F. Bonnier, J. Lee, P. Dumas and P. Gardner, Analyst **134** (8), 1586-1593 (2009).

[15] R. D. L. Kronig, J. Opt. Soc. Am. **12** (6), 547-556 (1926).

[16] H. A. Kramers, (presented at the Atti Cong. Intern. Fisica, (Transactions of Volta Centenary Congress) Como (unpublished), 1927).

[17] R. Bhargava, Appl Spectrosc **66** (10), 1091-1120 (2012).

[18] B. J. Davis, P. S. Carney and R. R. Bhargava, Analytical Chemistry **82**, 3474–3486 (2010).

[19] B. J. Davis, P. S. Carney and R. R. Bhargava, Analytical Chemistry **82**, 3487–3499 (2010).

[20] P. Bassan, A. Kohler, H. Martens, J. Lee, H. J. Byrne, P. Dumas, E. Gazi, M. Brown, N. Clarke and P. Gardner, Analyst **135** (2), 268-277 (2010).

[21] P. Bassan, A. Kohler, H. Martens, J. Lee, E. Jackson, N. Lockyer, P. Dumas, M. Brown, N. Clarke and P. Gardner, J Biophotonics **3** (8-9), 609-620 (2010).

[22] P. Bassan, A. Sachdeva, A. Kohler, C. Hughes, A. Henderson, J. Boyle, J. H. Shanks, M. Brown, N. W. Clarke and P. Gardner, Analyst **137** (6), 1370-1377 (2012).

[23] B. Bird, M. Miljkovic and M. Diem, Journal of Biophotonics **3** (8-9), 597-608 (2010).

[24] M. Miljkovic, B. Bird and M. Diem, Analyst **137** (17), 3954-3964 (2012).

[25] J. L. Ilari, M. Martens and T. Isaksson, Appl Spectrosc **42** (5), 722-728 (1988).

[26] H. C. v. d. Hulst, Light scattering by small particles. (Wiley, New York,, 1957).

[27] G. L. Carr, L. M. Miller and P. Dumas, in Biomedical Applications of Synchrotron Infrared Microspectroscopy, edited by D. Moss (Royal Society of Chemistry, 2011).

[28] C. F. Bohren and D. R. Huffman, in Absorption and Scattering of Light by Small Particles (Wiley-VCH Verlag GmbH, 2007), pp. 475-476.
[29] P. Dumas, F. Polack, B. Lagarde, O. Chubar, J. L. Giorgetta and S. Lefrancois, Infrared Phys Techn **49** (1-2), 152-160 (2006).
[30] P. Chýlek, J. Opt. Soc. Am. **66** (3), 285-287 (1976).
[31] P. Chýlek, J. T. Kiehl and M. K. W. Ko, Appl Optics **17** (19), 3019-3021 (1978).
[32] S. K. Mas Rosemal H. Mas Haris, S. Mohanc, Der Pharma Chemica **2** (4), 316-323 (2010).
[33] D. J. Griffiths, Introduction to Electrodynamics, 3 ed. (Prentice-Hall, Upper Saddle River, 1999).
[34] W. W. Parson, Modern Optical Spectroscopy, Student Edition ed. (Springer, Heidelberg, 2009).

Figure captions:

Figure 1 Illustration of the scattering of incident light with intensity I_0 at an arbitrary-shaped absorbing scatterer. A plane wave is incident from the left. In general, part of the incident light is scattered into different directions, part of the light is chemically absorbed by the scatterer, and part of the incident light is transmitted to the detector. The part of the incident infrared light chemically absorbed by the scatterer is indicated by the red area, representing a radiation sink.

Figure 2 (a) Apparent absorbance spectrum (red curve) for a sphere assuming a single absorption band located at 1654 cm^{-1}, corresponding to the C=O stretching vibration of the peptide bond in proteins. As parameters for the calculation of the refractive index, according to the Lorentz model (see Appendix A), $\Lambda = 10^4\ cm^{-2}$, $\Gamma = 30\ cm^{-1}$ and $\bar{\varepsilon}_r = 1.44$ were chosen (corresponding to a background refractive index of 1.2). The apparent absorbance spectrum with complex index of refraction is compared to an approximation of the absorbance with real index of refraction (blue curve) often found in the literature, assuming that absorbance and extinction are proportional. (b) Enlarged subfigure of (a) in the spectral range of the absorption band.

Figure 3 Apparent absorbance spectrum of the absorbing sphere of Fig. 2 (red) is compared to the *apparent absorbance* (blue) according to Bassan et al. [14]. Compared with the result considering complex index of refraction, the *apparent absorbance* considering real index of refraction is shifted to a lower frequency.

Figure 4 Extinction efficiency in the forward direction and scattering efficiency, including a numerical aperture, for a 10µm radius sphere assuming a single absorption band located at 1654 cm^{-1} for two cases $\Lambda = 10^4\ cm^{-2}$, $\Gamma = 30\ cm^{-1}$ and $\bar{\varepsilon}_r = 1.3$ (corresponding to an n_0=1.14) (a) and $\Lambda = 10^4\ cm^{-2}$, $\Gamma = 30\ cm^{-1}$ and $\bar{\varepsilon}_r = 1.54$ (corresponding to an n_0=1.24) (b).

Figure 5 Synchrotron spectrum of a PMMA sphere with radius 10µm (a), in the wavenumber range 3600-7200 cm^{-1} (b); in the wavenumber range 800-3600 cm^{-1} (c) and zoomed in the wavenumber range 5850-7000 cm^{-1} (d).

Figure 6 Root mean square error (RMSE) as a function of size factor α for the spectrum of a PMMA sphere shown in Fig. 5b. Inset: RMSE function in the vicinity of the four main local minima.

Figure 7 Measured absorbance and predicted absorbance for $\alpha = 0.64\mu m$ (a), $\alpha = 1.1\mu m$ (b), $\alpha = 2.1\mu m$ (c) and $\alpha = 3.1\mu m$ (d) .

Figure 8 Imaginary part of the complex refractive index for three different values of n_0 and a after 12 iterations.

Figure 9 Predicted absorbance for three different values of n_0 and a after 12 iterations.

Figure 10 Calculated pure absorbance spectrum of a PMMA thin film with thickness d_{eff}=5.9μm and the imaginary part of refractive index obtained with the van Dijck iterative algorithm.

Figure 11 *Juniperus chinensis* pollen synchrotron FTIR spectrum (a). Synchrotron FTIR spectra of *Juniperus chinensis* pollen ranging from 3600 cm^{-1} to 6300 cm^{-1} (b); from 1000 cm^{-1} to 3600 cm^{-1} (c) and from 1880 cm^{-1} to 2771 cm^{-1}(d).

Figure 12 Root mean square error (RMSE) as a function of α for the spectrum of a *Juniperus chinensis* pollen grain shown in Fig. 11b. The inset shows the RMSE function in the vicinity of the four main local minima.

Figure 13 Measured absorbance and predicted absorbance for $\alpha = 1.0\mu m$ (a), $\alpha = 1.3\mu m$ (b), $\alpha = 2.2\mu m$ (c) and $\alpha = 3.2\mu m$ (d) .

Figure 14 Root mean square error as a function of size parameter for a *Juniperus chinensis* pollen grain, considering the measured spectrum in the range between 1880 cm^{-1} and 2771 cm^{-1}.

Figure 15 Imaginary part of the complex refractive index for two different values of n_0 and a after 20 iterations.

Figure 16 Predicted absorbances for two different values of n_0 and a after 20 iterations.

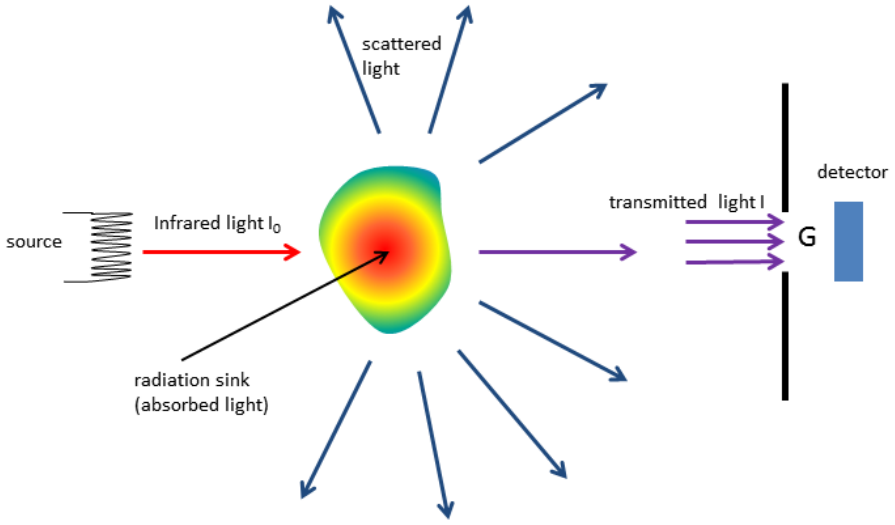
scattered
light
source
Infrared light I_0
transmitted light I
detector
G
radiation sink
(absorbed light)

Fig. 1

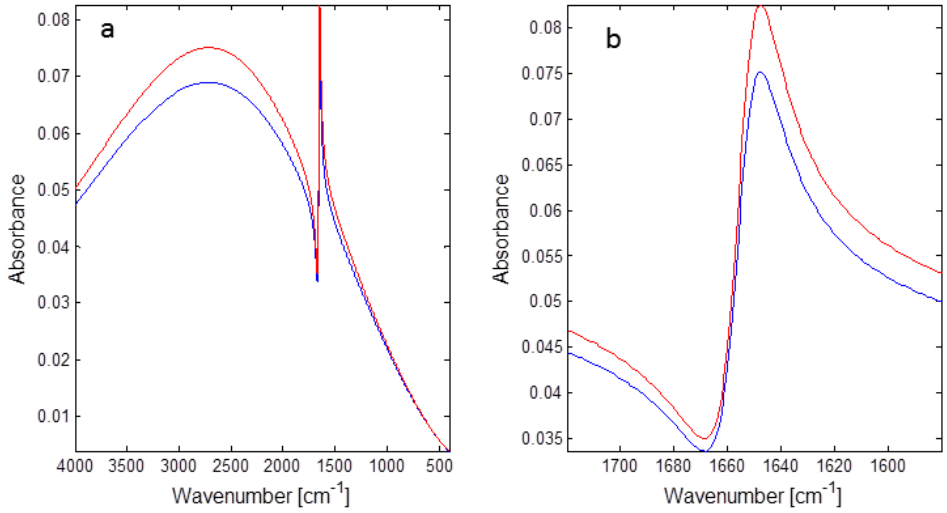
a
b
Absorbance
Wavenumber [cm-1]
0.08
0.07
0.06
0.05
0.04
0.03
0.02
0.01
4000 3500 3000 2500 2000 1500 1000 500
0.08
0.075
0.07
0.065
0.06
0.055
0.05
0.045
0.04
0.035
1700 1680 1660 1640 1620 1600

Fig. 2

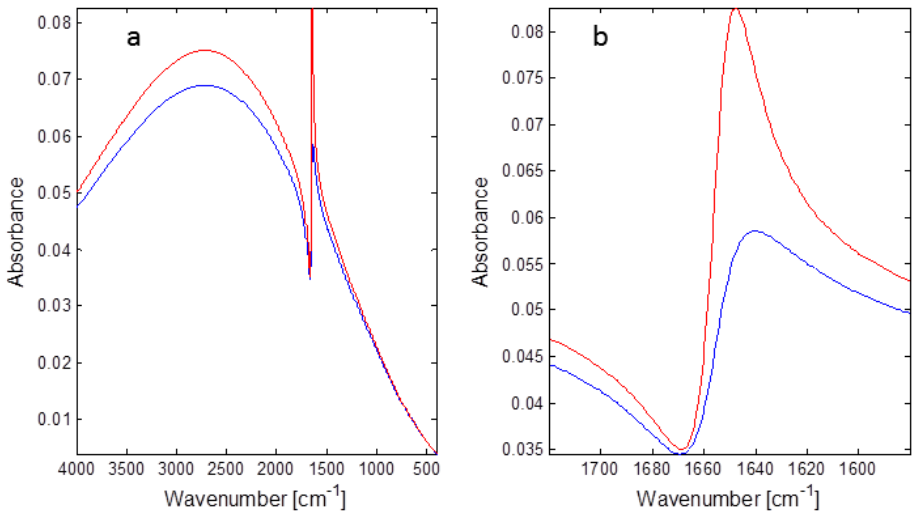
a
b
Absorbance
Wavenumber [cm-1]
0.08
0.07
0.06
0.05
0.04
0.03
0.02
0.01
4000 3500 3000 2500 2000 1500 1000 500
0.08
0.075
0.07
0.065
0.06
0.055
0.05
0.045
0.04
0.035
1700 1680 1660 1640 1620 1600

Fig. 3

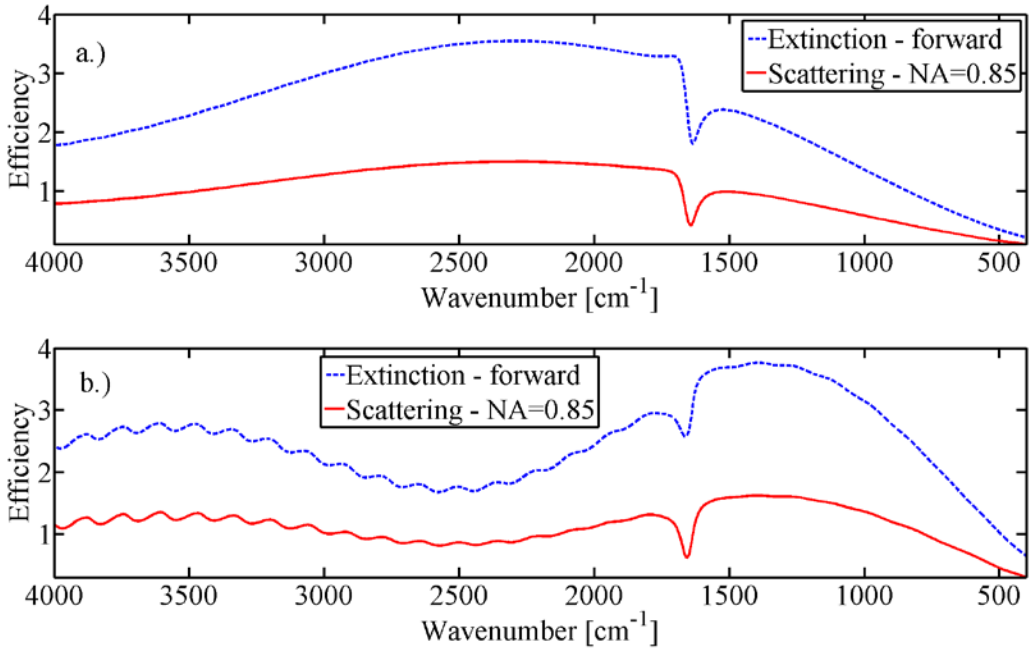
a.)
Extinction - forward
Scattering - NA=0.85
Efficiency
Wavenumber [cm-1]
b.)
Extinction - forward
Scattering - NA=0.85
Efficiency
Wavenumber [cm-1]

Fig. 4

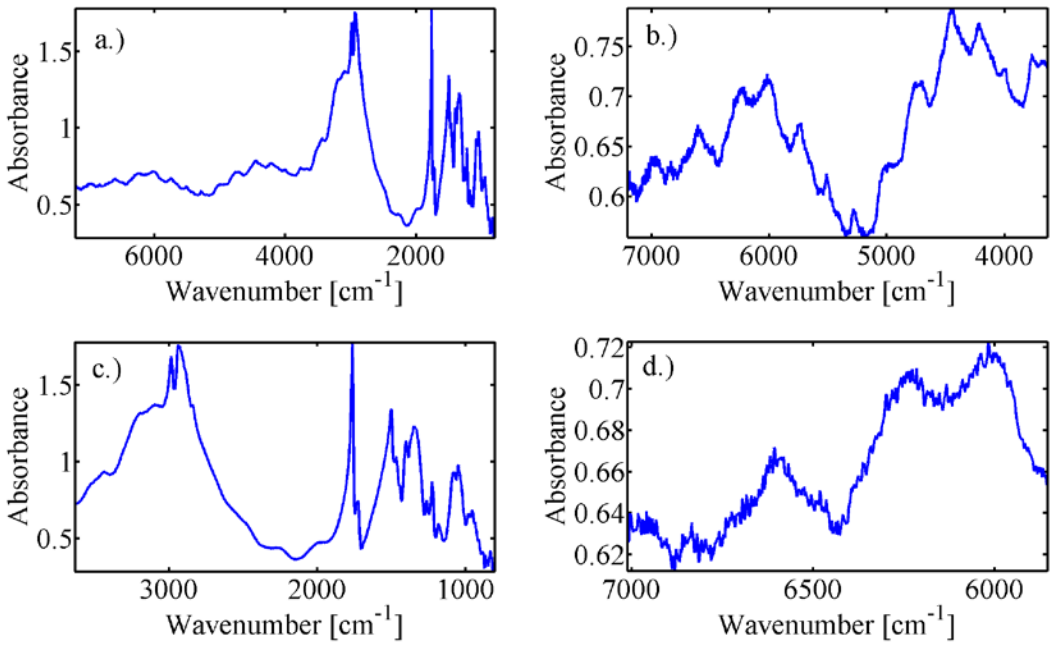
a.)
Absorbance
1.5
1
0.5
6000
4000
2000
Wavenumber [cm-1]
b.)
Absorbance
0.75
0.7
0.65
0.6
7000
6000
5000
4000
Wavenumber [cm-1]
c.)
Absorbance
1.5
1
0.5
3000
2000
1000
Wavenumber [cm-1]
d.)
Absorbance
0.72
0.7
0.68
0.66
0.64
0.62
7000
6500
6000
Wavenumber [cm-1]

Fig. 5

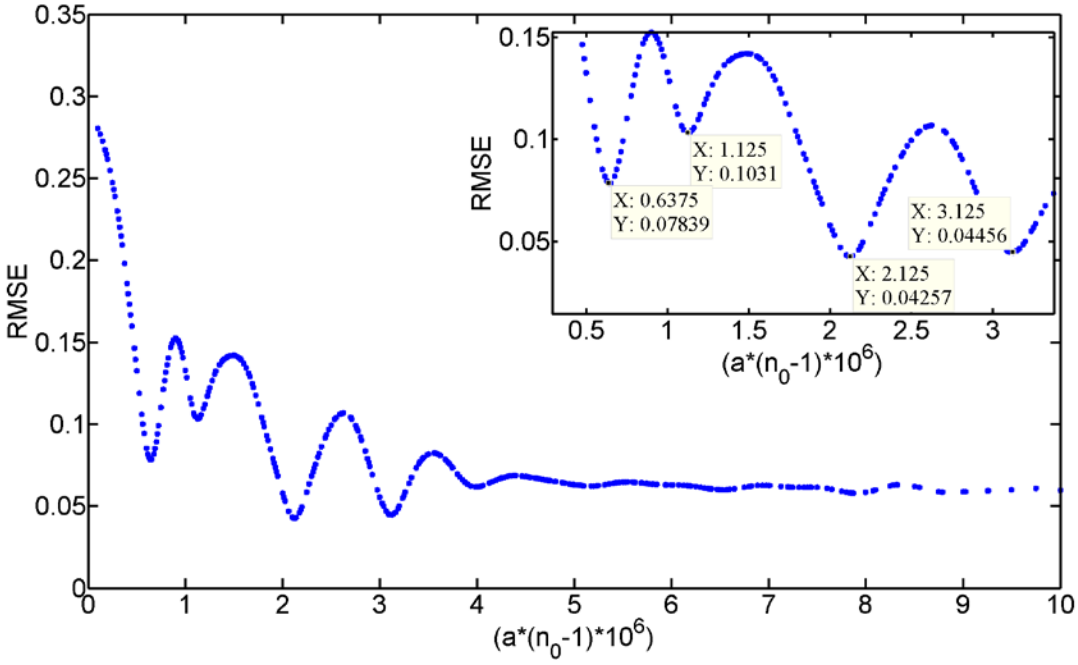
RMSE
(a*(n0-1)*10^6)
X: 0.6375
Y: 0.07839
X: 1.125
Y: 0.1031
X: 2.125
Y: 0.04257
X: 3.125
Y: 0.04456

Fig. 6

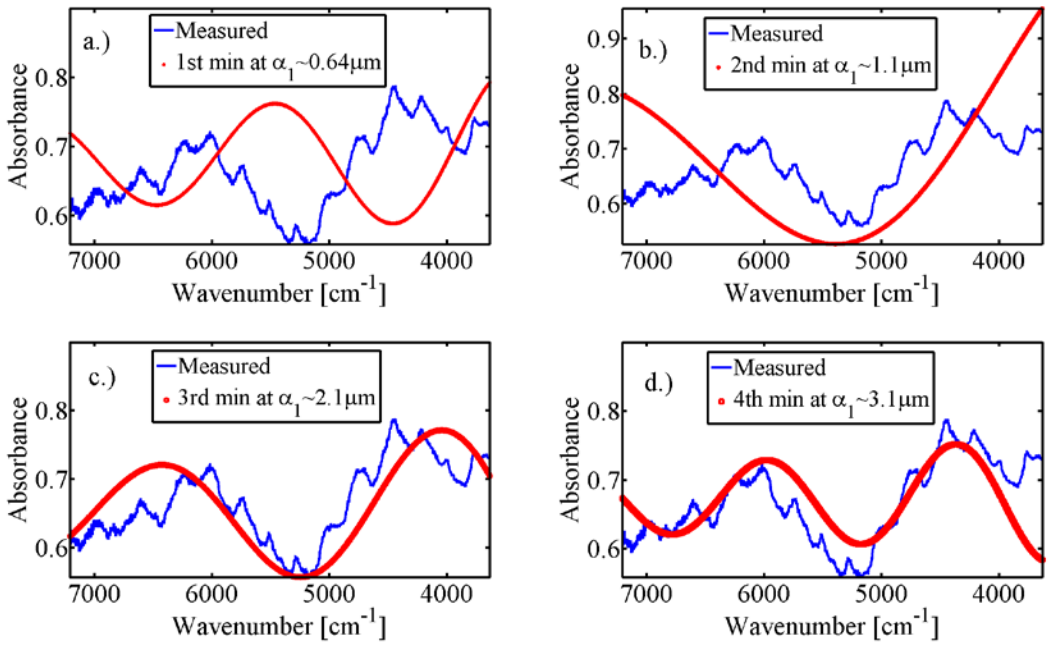
a.)
Measured
1st min at α1~0.64μm
b.)
Measured
2nd min at α1~1.1μm
c.)
Measured
3rd min at α1~2.1μm
d.)
Measured
4th min at α1~3.1μm
Absorbance
Wavenumber [cm-1]

Fig. 7

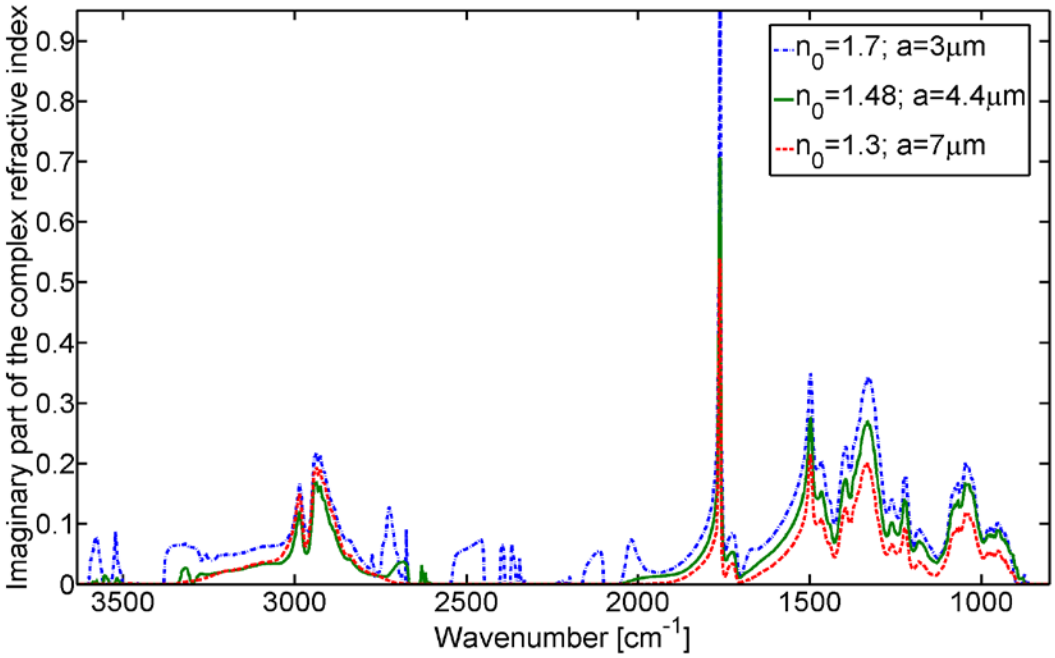
Imaginary part of the complex refractive index
0
0.1
0.2
0.3
0.4
0.5
0.6
0.7
0.8
0.9
3500
3000
2500
2000
1500
1000
Wavenumber [cm^{-1}]
n_0=1.7; a=3μm
n_0=1.48; a=4.4μm
n_0=1.3; a=7μm

Fig. 8

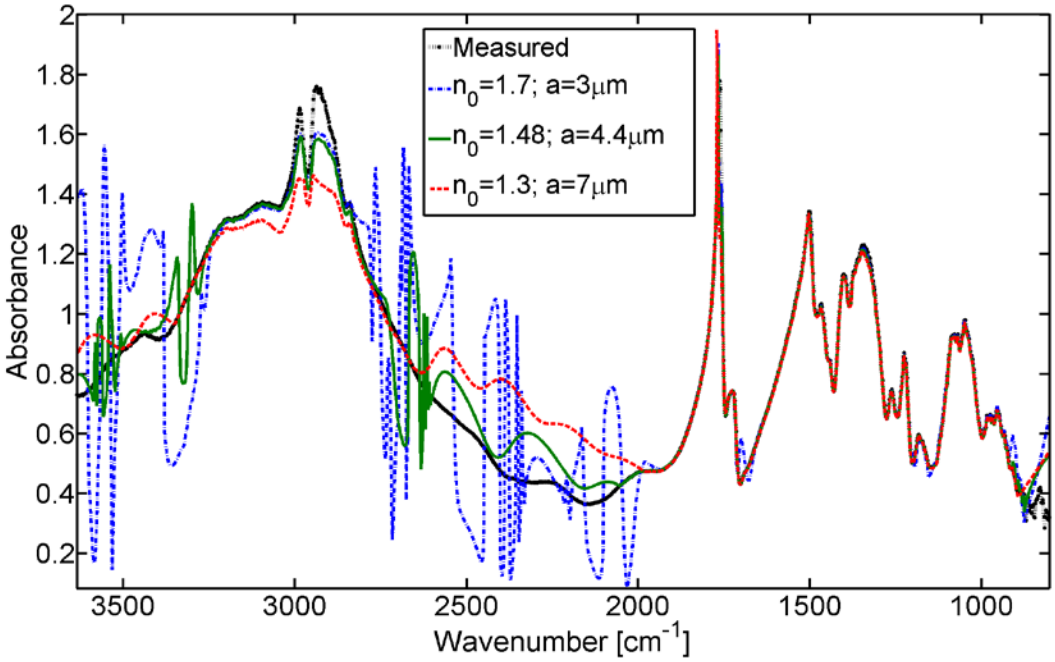
Measured
n0=1.7; a=3μm
n0=1.48; a=4.4μm
n0=1.3; a=7μm
Absorbance
Wavenumber [cm-1]
2
1.8
1.6
1.4
1.2
1
0.8
0.6
0.4
0.2
3500
3000
2500
2000
1500
1000

Fig. 9

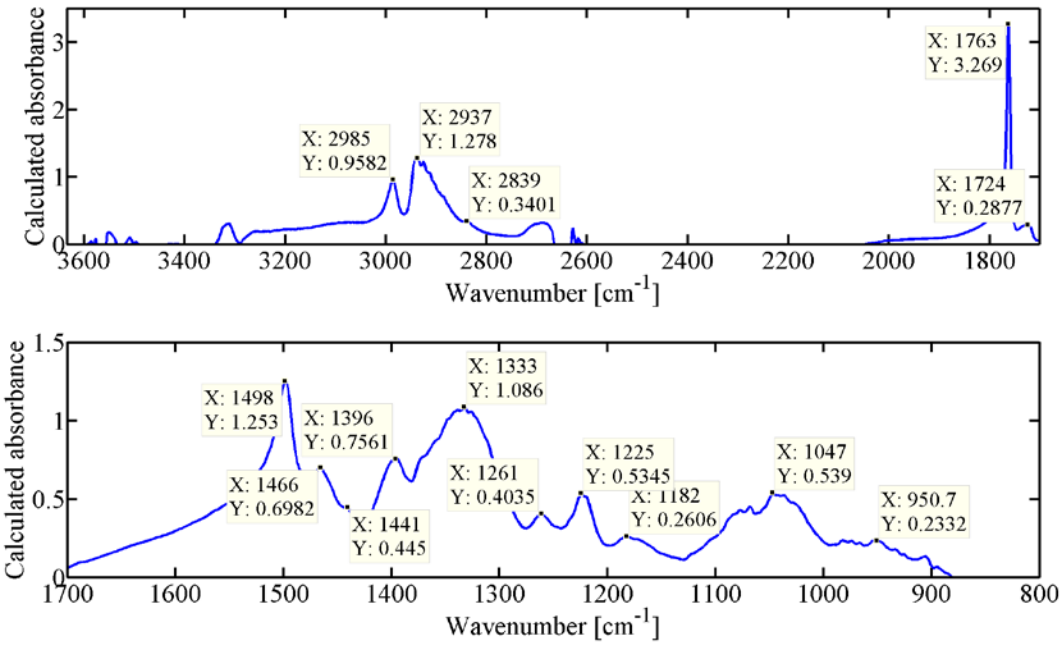
Calculated absorbance
Wavenumber [cm-1]
X: 1763
Y: 3.269
X: 2985
Y: 0.9582
X: 2937
Y: 1.278
X: 2839
Y: 0.3401
X: 1724
Y: 0.2877
X: 1498
Y: 1.253
X: 1396
Y: 0.7561
X: 1333
Y: 1.086
X: 1466
Y: 0.6982
X: 1441
Y: 0.445
X: 1261
Y: 0.4035
X: 1225
Y: 0.5345
X: 1182
Y: 0.2606
X: 1047
Y: 0.539
X: 950.7
Y: 0.2332

Fig. 10

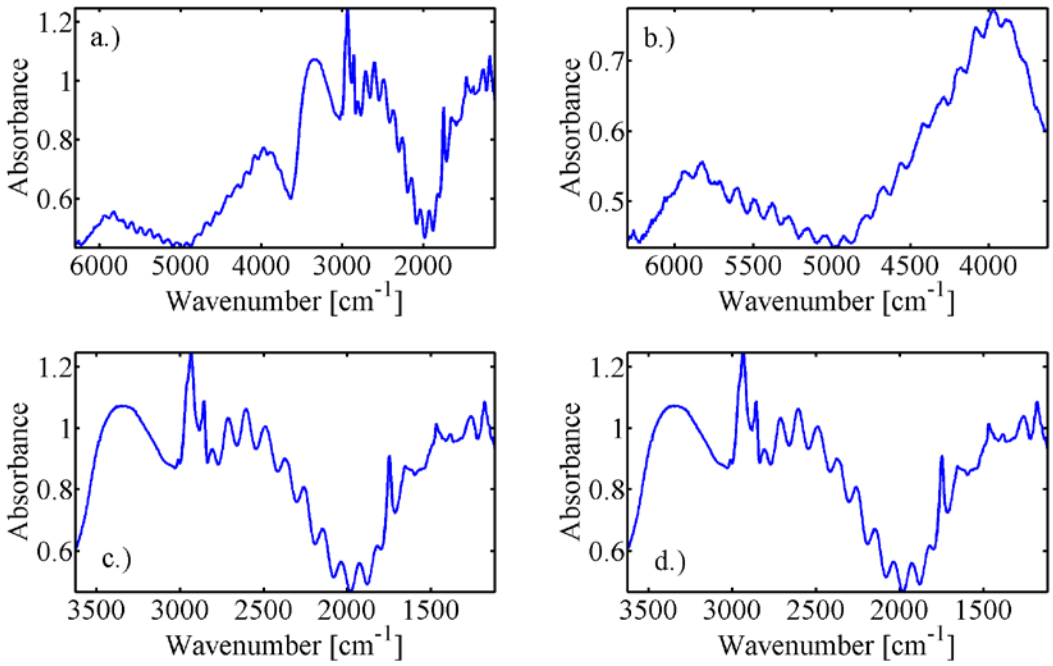
a.)
b.)
c.)
d.)
Absorbance
Wavenumber [cm-1]
1.2
1
0.8
0.6
0.7
0.5
6000 5000 4000 3000 2000
6000 5500 5000 4500 4000
3500 3000 2500 2000 1500

Fig. 11

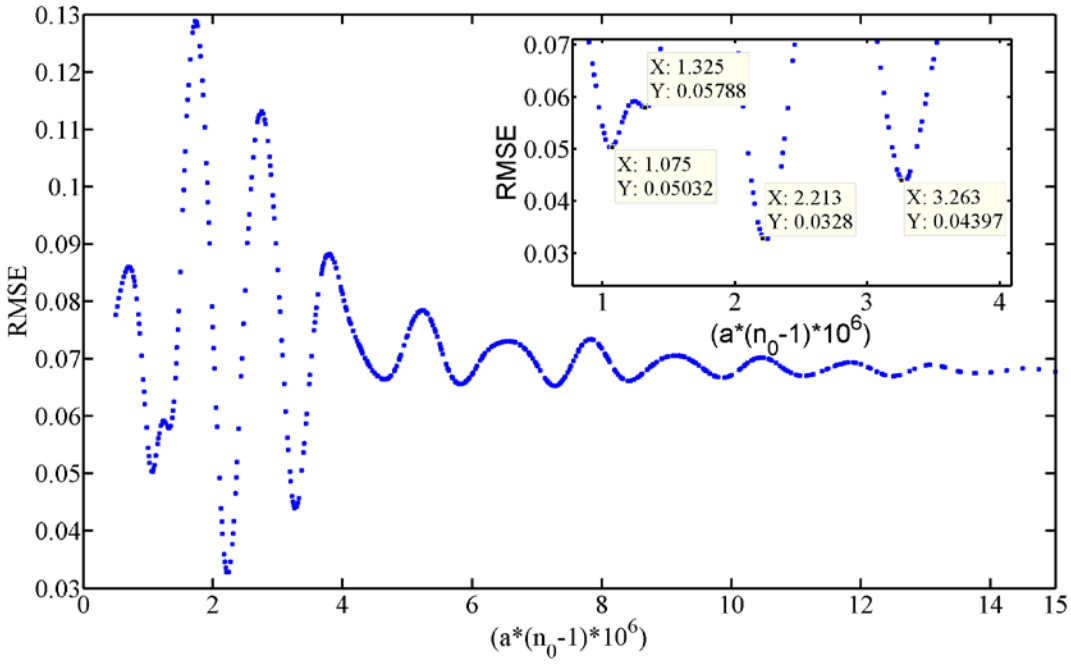
RMSE
(a*(n0-1)*10^6)
X: 1.325
Y: 0.05788
X: 1.075
Y: 0.05032
X: 2.213
Y: 0.0328
X: 3.263
Y: 0.04397

Fig. 12

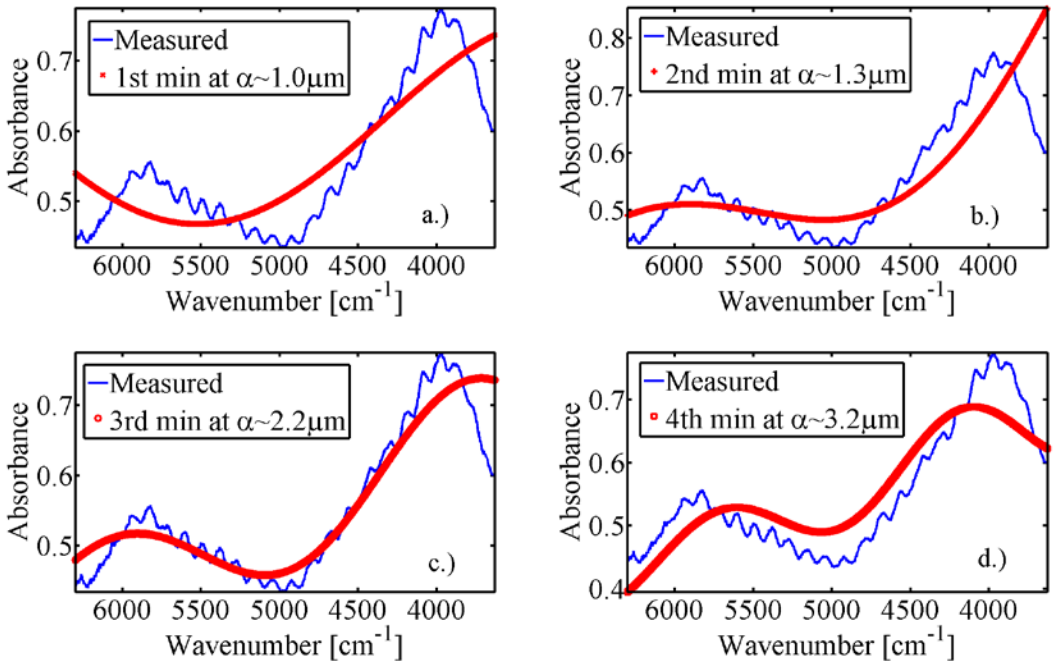
Measured
1st min at α~1.0μm
a.)
Absorbance
Wavenumber [cm-1]
Measured
2nd min at α~1.3μm
b.)
Absorbance
Wavenumber [cm-1]
Measured
3rd min at α~2.2μm
c.)
Absorbance
Wavenumber [cm-1]
Measured
4th min at α~3.2μm
d.)
Absorbance
Wavenumber [cm-1]

Fig. 13

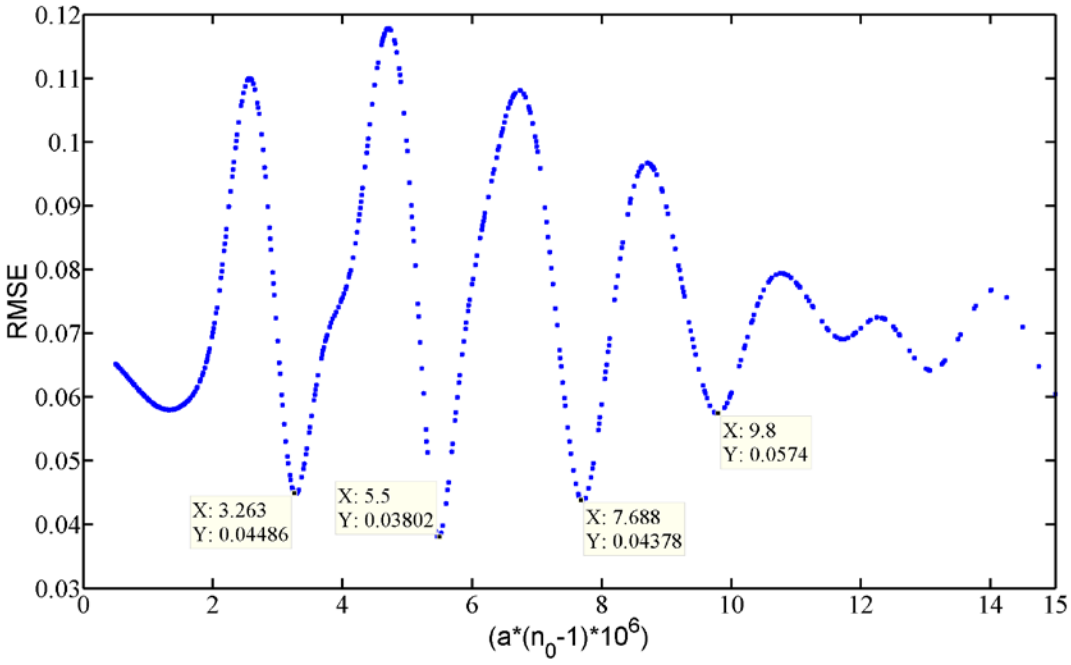
RMSE
(a*(n0-1)*10^6)
X: 3.263
Y: 0.04486
X: 5.5
Y: 0.03802
X: 7.688
Y: 0.04378
X: 9.8
Y: 0.0574

Fig. 14

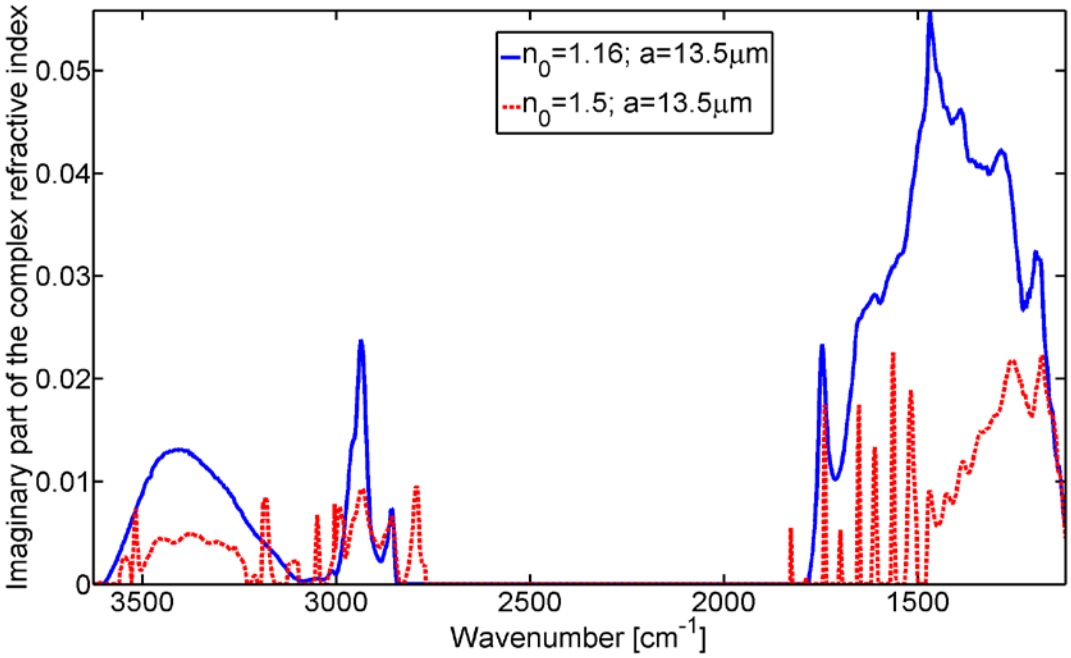
Imaginary part of the complex refractive index
0
0.01
0.02
0.03
0.04
0.05
3500
3000
2500
2000
1500
Wavenumber [cm-1]
n0=1.16; a=13.5μm
n0=1.5; a=13.5μm

Fig. 15

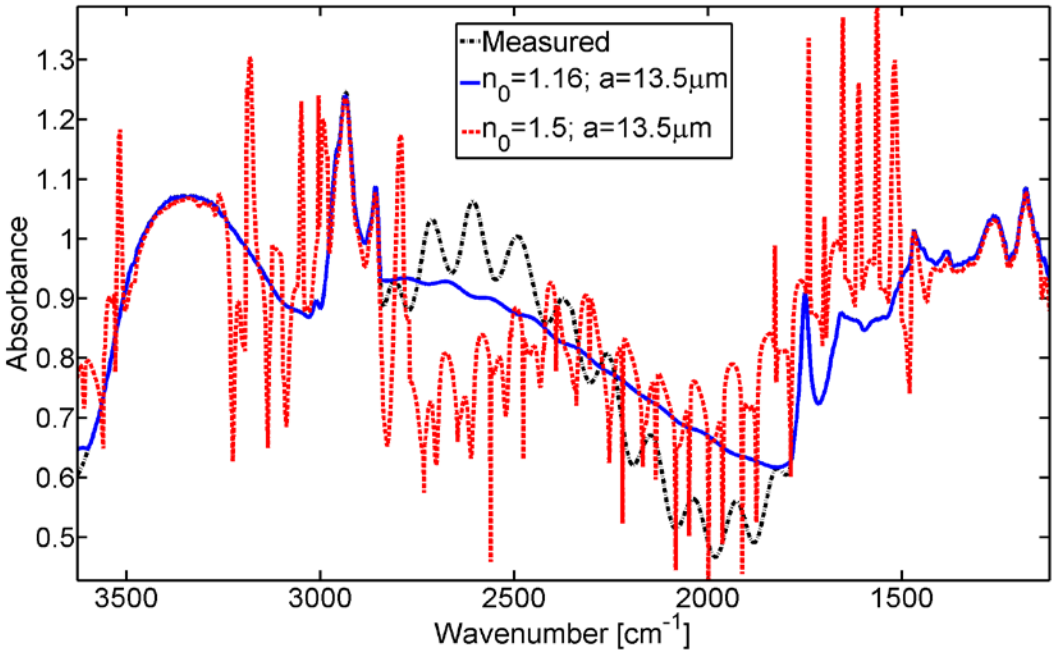
Measured
n0=1.16; a=13.5μm
n0=1.5; a=13.5μm
Absorbance
Wavenumber [cm-1]
1.3
1.2
1.1
1
0.9
0.8
0.7
0.6
0.5
3500
3000
2500
2000
1500

Fig. 16